Micron xxx (xxxx) 103743

Contents lists available at ScienceDirect

Micron

journal homepage: www.elsevier.com/locate/micron

Poly(L-lactide)/nano-hydroxyapatite piezoelectric scaffolds for tissue engineering

Angelika Zaszczyńska [a], Arkadiusz Gradys [a], Dorota Kołbuk [a], Konrad Zabielski [a], Piotr Szewczyk [b], Urszula Stachewicz [b], Paweł Sajkiewicz [a, *]

[a] Institute of Fundamental Technological Research, Polish Academy of Sciences, Pawinskiego 5B, Warsaw 02-105, Poland
[b] Faculty of Metals Engineering and Industrial Computer Science, AGH University of Krakow, Krakow 30-059, Poland

ARTICLE INFO

Keywords:
Scaffolds
Tissue engineering
Bone tissue engineering
Smart medicine
Biodegradable polymers
Regenerative medicine

ABSTRACT

The development of bone tissue engineering, a field with significant potential, requires a biomaterial with high bioactivity. The aim of this manuscript was to fabricate a nanofibrous poly(L-lactide) (PLLA) scaffold containing nano-hydroxyapatite (nHA) to investigate PLLA/nHA composites, particularly the effect of fiber arrangement and the addition of nHA on the piezoelectric phases and piezoelectricity of PLLA samples. In this study, we evaluated the effect of nHA particles on a PLLA-based electrospun scaffold with random and aligned fiber orientations. The addition of nHA increased the surface free energy of PLLA/nHA (42.9 mN/m) compared to PLLA (33.1 mN/m) in the case of aligned fibers. WAXS results indicated that at room temperature, all the fibers are in an amorphous state indicated by a lack of diffraction peaks and amorphous halo. DSC analysis showed that all samples located in the amorphous/disordered alpha' phase crystallize intensively at temperatures just above the T_g and recrystallize on further heating, achieving significantly higher crystallinity for pure PLLA than for doped nHA, 70 % vs 40 %, respectively. Additionally, PLLA/nHA fibers show a lower heat capacity for PLLA in the amorphous state, indicating that nHA reduces the molecular mobility of PLLA. Moreover, piezoelectric constant d_{33} was found to increase with the addition of nHA and for the aligned orientation of the fibers. *In vitro* tests confirmed that the addition of nHA and the aligned orientation of nanofibers increased osteoblast proliferation.

1. Introduction

Over 1 million bone graft procedures are conducted annually in the United States (Huang et al., 2024; Wortham et al., 2024). Tissue engineering emerges as a potential avenue for effective bone repair (Zhang et al., 2024). Scaffolds intended for bone tissue engineering must have a structure similar to natural bone (Kennedy et al., 2024; Zaszczyńska et al., 2022) and be meticulously formed to facilitate osteogenic cell adhesion, proliferation, and differentiation (Bose et al., 2024; Pathak et al., 2023).

The requirements for cellular scaffolds in bone tissue engineering include several key aspects of effective bone growth, development, and regeneration (Bose et al., 2012). To provide adequate structural support, scaffolds can have a similar chemical composition and architecture similar to natural bone tissue (Chen et al., 2022). They must be biocompatible, meaning they should not cause negative immune reactions or toxicity when interfacing with surrounding cells (Fendi et al., 2024). This is crucial to avoid rejection and ensure safe use in living organisms. Additionally, the scaffold should gradually degrade, leaving space for the growth and regeneration of natural bone (Bauso et al., 2024; Manzini et al., 2021). Optimal scaffold microstructure and porosity allow nutrients, gases, and cells to diffuse through the scaffold. High porosity supports cell colonization and increases the effectiveness of regenerative processes (Liu et al., 2023). From the perspective of scaling from the laboratory to the industrial scale and widespread use, there should be the ease of fabrication of these scaffolds in a controlled manner, and the production process should be easy to scale to enable mass production for clinical applications (Norouzi et al., 2024; Zaszczyńska et al., 2024a).

PLLA exists in an amorphous or semi-crystalline form, exhibiting several desirable properties in tissue engineering (Khouri et al., 2024; Saurav et al., 2024; Srivastava et al., 2024). One of the possible applications is the area of bone tissue engineering, considering its favorable biocompatibility and biodegradability (Liu et al., 2024; Sethu et al., 2024). These features depend largely on the molecular conformation and the arrangement of polymer chains, which may vary depending on

* Corresponding author.
E-mail address: psajk@ippt.pan.pl (P. Sajkiewicz).

https://doi.org/10.1016/j.micron.2024.103743
Received 17 October 2024; Received in revised form 7 November 2024; Accepted 7 November 2024
0968-4328/

the PLLA crystal form (Hoogsteen et al., 1990; Zhang et al., 2010). PLLA shows complex polymorphism with three main crystalline forms: α (Eling et al., 1982; Puiggali et al., 2000), β (Eling et al., 1982; Puiggali et al., 2000; Glimcher, 1959), and γ (Cartier et al., 2000), depending on preparation conditions. Besides these three main crystal polymorphs, two disordered modifications of the α form, named α' and α'', were observed in PLLA (Zhang et al., 2005, 2006; Wasanasuk and Tashiro, 2011; Wunderlich and Grebowicz, 1984; Liu et al., 2014). According to the literature, the α' modification has a conformational disorder and a loose chain-packing manner, which makes this crystal modification a mesophase (condis crystal) (Liu et al., 2014; Pan et al., 2012; Barbosa et al., 2023; Zhang and Ma, 1999).

An ideal bone grafting material should exhibit osteoconductive, osteoinductive, and piezoelectric characteristics (Glimcher, 1959). Hydroxyapatite affects the piezoelectric properties of bone tissue. This is caused by shifts of ions in the crystal structure of nHA under mechanical stress, which leads to a change in the ionic balance and a dipole moment. Asymmetries in the structure allow the network to be polarized and an electrical signal generated. This piezoelectricity plays a key role in bone remodeling and tissue regeneration and is important for bone homeostasis (Barbosa et al., 2023). Hydroxyapatite is a crucial bioactive osteogenic inducer, playing a vital role in the adhesion of synthetic scaffolds to regenerating bone. The chemical integration between prosthetic biomaterials and bone tissue *in situ* can be accomplished by forming a layer of biologically active bone-like apatite on the surface of the scaffold (Zhang and Ma, 1999; Hong et al., 2008). Spherical nanoparticles exhibit the highest surface-to-volume ratio (Winey and Vaia, 2007). Due to their nanoscale dimensions, nearly spherical morphology, distinctive mechanical and physicochemical properties, surface chemistry, and excellent biocompatibility, nanoparticles integrated into a polymer matrix stand out as highly promising materials for multifunctional nanocomposites across diverse applications, including biomedical ones (Rancan et al., 2009; Rachmawati, 2016; Patel and Gundloori, 2023). The surface charges generated influence protein adsorption, affecting cell adhesion, migration, morphology, and proliferation. Polarized nHA accelerates protein adsorption, affecting cell adhesion, migration, morphology, proliferation, and the growth of bone-like apatite crystals in simulated body fluid (Saxena et al., 2019; Zhang et al., 2023a; Farag, 2023). Osteoblast cells exhibit enhanced proliferation on negatively polarized nHA surfaces, promoting new bone formation and enhanced osteobonding at injury sites. Furthermore, polarized nHA aids in the regeneration of blood vessels and epidermis during wound healing (Nagai et al., 2008; Okabayashi et al., 2009).

Considering the diverse range of potential applications for electrospun mats, including biomedical (Baniasadi et al., 2023), environmental (Zhou et al., 2023), and electronic applications (Li et al., 2024), one of the significant challenges in the electrospinning approach lies in preparing mats with adjustable properties (Xing et al., 2023). In this context, various modifications, both during the process and post-process of electrospun mats, have been suggested (Yang et al., 2023). These modifications encompass the use of multiple jets, fiber alignment, coaxial electrospinning, surface modifications, blending with other biopolymers, and/or incorporating micro or nanoparticles as fillers for the polymer matrix (Behroozi et al., 2023; Wang et al., 2023). Composite and nanocomposite materials have widespread applications across various fields, such as sensors, energy, anticorrosion, and catalysis. The ultimate properties of polymer-based composites are significantly influenced by various factors related to the interaction between the matrix and particles, including structure anisotropy and particle dimensions (Karbowniczek et al., 2022; Moradi et al., 2023; Szewczyk et al., 2023).

PLLA and nHA are materials widely used in tissue engineering, especially in the context of bone and nervous tissue regeneration. There are studies in the literature that analyze the effect of nHA on the properties of PLLA and its application in biomedicine. Li et al. investigated the properties of PLLA and nHA composites prepared by melt electrospinning (Li et al., 2012). Diaz et al. investigated the properties of materials made of PLLA/nHA in the form of polymer films (Díaz et al., 2019). *In vivo,* tests of printed materials made of PLLA with the addition of nHA were also carried out (Chen et al., 2019). However, only a few studies in the literature relate to PLLA nanofibers with the addition of nHA, e.g., (Tazibt et al., 2023; Davachi et al., 2016; Hwangbo et al., 2022). PLLA and nHA were selected for this study because of their complementary properties that make them suitable for tissue engineering applications, particularly for bone regeneration. The main advantage of this material system is thai it is a combination of biocompatibility and biodegradability, ability to mimic the natural composition of bone, and piezoelectric properties that is particularly crucial for bone tissue perspective. In our article, we propose an innovative approach to the electrospinning process, more precisely, the production of samples with random and aligned orientation of nanofibers. To summarize, the aim of the work was to investigate PLLA/nHA composites, particularly the effect of the fiber arrangements and the addition of nHA on the content of piezoelectric phases and piezoelectricity of PLLA samples. There are no works analyzing the piezoelectricity of PLLA materials with the addition of nHA in the context of piezoelectric properties occurring in natural bone. Our hypothesis was that even in the case of semicrystalline PLLA, nHA amplifies the piezoelectricity of the obtained fibers. Additionally, there is a lack of data on the influence of fiber arrangement on piezoelectricity in the context of cellular growth and viability. Osteoconductivity was examined using osteoblasts to evaluate the suitability of PLLA/nHA composites in bone tissue engineering.

2. Materials and methods

2.1. Materials

Poly(L-lactide) (PLLA, Purasorb PL 49, Corbion), with molecular weight Mw - 330 000 g/mol, was purchased from Purac, Netherlands. Nano-hydroxyapatite (nHA), a nanopowder $<$200 nm particle, was purchased from Sigma-Aldrich, Germany. 1,1,1,3,3,3, -hexafluoro-2-propanol (HFIP) was purchased from Iris Biotech GmbH, Germany. All chemical reagents were analytically pure.

Reagents for *in vitro* tests, such as amino acids, L-glutamine, fetal bovine serum (FBS), and antibiotics (penicillin/streptomycin), were purchased from Sigma Aldrich, Germany. Phosphate-buffered saline (PBS), Presto Blue, Trypsin EDTA, Dulbecco's Modified Eagle Medium, ActinGreen, and NucBlue were purchased from Thermo Fisher Scientific, United States. The cell line osteoblasts MG-63 were purchased from Sigma-Aldrich, Germany.

2.2. Preparation of PLLA solution, PLLA/nHA solution, and nanofibrous scaffold formation

PLLA fibers were formed using electrospinning. PLLA pellets were dissolved in HFIP at room temperature and left overnight. For electrospinning, 3.5 w/v % of PLLA solutions were prepared. Subsequently, the solution was doped with nHA at a 10 % w/v concentration. To prevent aggregation of the nHA nanoparticles, the solutions were treated with ultrasound (ultrasonic cleaner EMAG, EMMI-D60, Germany) for 20 min.

All PLLA solutions were loaded into a 3 ml syringe and positioned in an electrospinning chamber (Fluidnatek LE-50, Bioinicia, Valencia, Spain). The solutions were dispensed through 23-gauge stainless steel needles with an inner diameter of 0.337 mm at a flow rate of 1.5 ml/h. The distance from the needle tip to the collector was 110 mm. Fibers were gathered on a rotating drum collector (50 mm radius and 70 mm length) at rotation speeds of 200 rpm for random fibers and 2000 rpm for oriented fibers, with a linear velocity of 5.16 m/s. The process was conducted at temperatures between 21°C and 23°C and relative humid-

ity of 30 %. A positive voltage of 11 kV was applied to the needle while the collector was kept at a potential of −2 kV. After electrospinning, all materials were placed under a fume hood for 24 h to allow solvent residues to evaporate. The samples were named in analogy to the composition and speed of the collector during the manufacturing process; more precisely, PLLA formed at low rotational speed (100 rpm) was named PLLA_R (random orientation of fibers), and those formed at high rotational speed (2000 rpm) were named PLLA_A (aligned orientation of fibers). In the case of hydroxyapatite addition, nHA was added to the sample name; for example, PLLA/nHA_R means a hydroxyapatite-added sample formed at low collector speed (100 rpm), and PLLA/nHA_A means a hydroxyapatite-added sample formed at high collector speed (2000 rpm).

2.3. Characterization of PLLA/nHA nanofibrous scaffolds

2.3.1. Morphology analysis

Scanning electron microscopy (SEM) imaging was used to analyze the morphology using an accelerating voltage of 10 kV (SEM, JSM-6010PLUS/LV InTouchScope™, JEOL, Tokyo, Japan). Before imaging, each nonwoven underwent gold coating (approx. 10 nm) (Smart Coater, JEOL, Tokyo, Japan). Data analysis was conducted using ImageJ software (1.52q software version). The fiber diameter distribution was determined by employing a Gaussian approximation with 100 measurements per sample, and the goodness fit was also provided using ImageJ software

The impact of the collector's rotational speed on fiber orientation within the nanofibrous scaffold was analyzed using the directionality plugin in ImageJ software. Fourier Transform was applied to segments of the SEM images to determine the orientation patterns. The orientation distribution was then approximated with a Gaussian function using Origin 2021b software. The degree of fiber alignment was further evaluated by calculating the full width at half maximum (FWHM) of the Gaussian function used for the orientation distribution approximation. FWHM values were averaged across five images for each sample (Hotaling et al., 2015).

The orientation factor was determined using the anisotropy index α, where α equals 1 indicates perfect alignment and α = 0 represents a random distribution (Eqs. (1),(2)) (Shehata et al., 2018):

$$\Omega = \frac{1}{I_{tot}} \sum I_i \begin{vmatrix} \cos^2\theta_i & \sin\theta_i \cos\theta_i \\ \sin\theta_i \cos\theta_i & \sin^2\theta_i \end{vmatrix} \quad (1)$$

$$\alpha = 1 - \lambda_1/\lambda_2 \quad (2)$$

where Ω represents the orientation matrix with eigenvalues of λ_1 and λ_2, I_{tot} - is the total length of the nanofiber (nm), I_i- is the length of the individual i-th nanofiber (nm), θ_i- angle between the nanofiber and the x-axis. The lengths and angles of the nanofibers were measured from SEM images using the Directionality plugin in ImageJ software.

Total average porosity (p) was determined from Eq. (3) (Zaszczyńska et al., 2024a):

$$p = \frac{V_t - V_f}{V_t} = \left(1 - V_f \times \frac{\rho}{m_t}\right) = \left(1 - \frac{m_f}{m_t}\right) \quad (3)$$

Where m_t is the theoretical mass of the solid sample, calculated as the product of the volume occupied by a patch V_t and the density of PLLA (1.25 g/cm^3) (Wang et al., 2007), while V_f and m_f denote the actual sample volume and mass, respectively.

The average pore size (p) was calculated from Eq. 4 (Zaszczyńska et al., 2024a):

$$P = \frac{2D}{(1-p)} \quad (4)$$

where, p is approximately the total porosity, D - the mean fiber diameter, $(1 - p)$ - average total area of fibers per unit area.

Energy Dispersive X-ray Spectroscopy (EDS) was used to confirm the presence of nHA (JSM-6010PLUS/LV InTouchScope™, JEOL, Tokyo, Japan). Samples were measured with the following parameters: accelerating voltage of 8 kV, working distance (WD) = 10 mm, probe current = 500 pA, and a collecting time of 30 min. The EDS analysis of the distribution of oxygen (O), phosphorus (P), calcium (Ca), and carbon (C) was performed.

2.3.2. Water contact angle measurements, surface tension energy, and water uptake determination

The water contact angle (WCA) of all nanofibrous samples was assessed using the static water contact angle method. Measurements were performed with a Data Physics OCA 15EC contact angle goniometer (Filderstadt, Germany). A distilled water droplet (2 μl) was placed on the nanofibrous scaffold surface at room temperature, and the water contact angle was recorded after 3 s. Each measurement was repeated 10 times for each type of material, and then the measurement was averaged.

The surface free energy (SFE) was specified using the Kaelble-Owens-Wendt method, which considers that the SFE consists of two main independent components: dispersion and polar interactions. Three liquids were used to calculate the surface free energy: diiodomethane, water, and formamide, according to the previously described procedure (Rudawska and Jacniacka, 2009; Kołbuk et al., 2022).

Components γ_s^p and γ_s^d of all samples can be calculated from Eq. 5 and Eq. 6:

$$(\gamma_s^d)^{0,5} = \frac{\gamma_d\left(\cos\theta_d + 1\right) - \sqrt{\left(\frac{\gamma_d^p}{\gamma_w^p}\right)}\gamma_w(\cos\theta_w + 1)}{2(\sqrt{\gamma_d^d} - \sqrt{\gamma_d^p - (\frac{\gamma_w^p}{\gamma_w^p})})} \quad (5)$$

$$(\gamma_s^p)^{0,5} = \frac{\gamma_w\left(\cos\theta_w + 1\right) - 2\sqrt{\gamma_s^d\gamma_w^d}}{2\sqrt{\gamma_w^p}} \quad (6)$$

where, γ_s^d is the dispersion element of Surface Free Energy of tested materials, and γ_s^p is the polar element of tested materials; γ^d Surface Free Energy of diiodomethane; γ_d^d the dispersive element of diiodomethane surface energy; γ_d^p the polar element of diiodomethane; γ_w Surface Free Energy of Water; $\gamma_w^d$the dispersive element of water Surface Free Energy; γ_w^ppolar element Surface Free Energy of water; θ_d and θ_w contact angle of diiodomethane and water.

Wu's method can be used to calculate the surface polarity (Xp) (Eq. 7) (Kleintjens, 2012):

$$X_p = \frac{\gamma_s^p}{\gamma_s} \quad (7)$$

The absorption capacity of the scaffolds was assessed by measuring their ability to take in water, which is primarily influenced by the materials' hydrophilic properties (Rai et al., 2005). Each scaffold was sectioned into 2 × 1 cm pieces and submerged in deionized water. After specific time intervals (60 s), the scaffolds were retrieved, softly dried with tissue paper, and weighed (analytical balance, XA 52.R2, Radwag, Poland). This procedure was repeated over 10 min. The water absorption rate was calculated using equation (Kleintjens, 2012):

$$\%Water\ uptake = 100 \times \frac{W_{wet} - W_o}{W_0} \quad (8)$$

where W_o is the dry weight of the sample, and W_{wet} is the weight of the wet sample.

2.3.3. Fourier transform infrared spectroscopy (FTIR)

Molecular structure analysis, including hydroxyapatite addition, was conducted using Fourier Transform Infrared Spectroscopy (FTIR-ATR, Bruker Vertex 70, Mannheim, Germany). The results were averaged from five independent samples and runs. The samples were scanned in the range of 400 cm^{-1} to 4000 cm^{-1} with a resolution of 2 cm^{-1} and a total of 32 scans.

2.3.4. Differential scanning calorimetry (DSC)

Thermal analysis of PLLA scaffolds, both pure and with nHA particles, was performed using a Differential Scanning Calorimeter Pyris 1 DSC (Perkin Elmer, Waltham, MA, USA) equipped with Intracooler 2 P under nitrogen atmosphere. Before DSC analysis, samples with masses 6–8 mg were loaded into standard aluminum pans and vacuum dried (vacuum dryer, Menmert, Spain) at ambient temperature for at least 24 hours to remove a solvent residue. DSC analysis consisted of two heating and cooling cycles at 10 K/min from −55ºC to 220ºC with 10 min fusion time. The scans were corrected for instrumental heat flow drift and curvature and are presented as apparent heat capacity, C_p, in $J/g_{PLLA}K$.

2.3.5. Wide angle X-ray scattering (WAXS)

Investigations were performed using a Bruker D8 Discover Diffractometer (Manheim, Germany). Measurements were conducted using Cu Kα radiation of wavelength λ = 1.5406 Å at a voltage of 40 kV and current of 40 mA. Measurements were conducted in reflection mode. Formation of the incident beam was performed using optics consisting of Göbel mirrors, a 1 mm linear slit, and a 2.5º n axial Soller. The WAXS profiles were recorded using a Lynxeye one-dimensional detector preceded by a Ni filter and a 2.5º axial Soller.

2.3.6. Piezoelectric coefficient measurements

The piezoelectric coefficient for electrospun PLLA membranes was evaluated using a specialized d_{33} meter (YE2730A d_{33} meter, Sinocera, China), tailored for precise measurements of d_{33} values in piezoelectric materials. Before the tests, electrodes of an 8 nm Au80–20Pd layer were sputter coated (Q150RS, Quorum Technologies, UK) on both sides of the PLLA fiber mats. Each sample was measured 5 times to obtain an average d_{33} value. A reference sample was integrated into the assessment process to ensure the instrument's accuracy and account for potential variations in piezoelectric values attributed to the high porosity of the materials (Sukumaran et al., 2023). This reference sample, obtained from PolyK (USA), was a piezoelectrically poled PVDF film measuring 110 μm in thickness, with a specified piezoelectric coefficient ranging from 23 to 28 pCN^{-1}. The 4 × 4 cm segment cut out from the reference sample was used for testing. The measurements were validated using the reference sample, yielding a value of 27.7 ± 1.5 pCN^{-1}, consistent with the manufacturer's reported range of 23–28 pCN^{-1}.

2.3.7. In vitro study

Biocompatibility tests were conducted using the human MG-63 cell line (86051601, Sigma Aldrich). The cells were cultured in a 25 cm^2 flask with a medium consisting of High Glucose Dulbecco's Modified Eagle's Medium (DMEM), 10 % fetal bovine serum (FBS), 1 % antibiotics, and 1 % glutamine. The cells were incubated in a 5 % CO2 environment at 37 °C. To detach the cells from the flask, they were washed with PBS. Subsequently, 3 ml of 0.05 % trypsin solution was added to the cells, and the flask was placed in the incubator for a few minutes. After harvesting the cells, 10 ml of culture medium was added, and centrifugation was performed at room temperature. The pellet was resuspended in a culture medium to achieve the required cell density. Various studies were conducted to assess the cellular response to monolithic nanofibers, including cytotoxicity on direct contact and cellular morphology after 3 and 5 days of cultivation.

For cellular viability assessment, the MG-63 cell suspension was seeded on samples and Tissue Culture Plate TCP with a density of 1×10^4 cells/well and placed in an incubator according to the previously described protocol (Zaszczyńska et al., 2024b). After 3 and 5 days, the culture medium was removed, and each well was filled with 180 ml of PBS and 20 ml of Presto blue reagent. Afterward, the plate was returned to the incubator for 60 min. Fluorescence was measured using 530/620 nm excitation/emission filters by Fluorescent Accent FL Thermo Fisher Scientific. The results were compared with the Presto Blue fluorescence of blank samples, indicating no metabolic activity, and the control (Tissue Culture Plate TCP), which exhibited 100 % viability.

Fluorescence microscopy was employed to verify MG-63 morphology in direct contact. MG-63 cells were seeded on electrospun membranes, and after 3 and 5 days of cultivation, cells were fixed in 3 % formaldehyde for 20 min. Fixed cells were then treated with 0.01 % Triton X 100 for 5 min to permeabilize cell membranes.

Finally, cellular nuclei and the cytoskeleton were stained for 30 minutes with a combined solution of ActinGreen and NucBlue. ActinGreen binds to the cytoskeleton, while NucBlue targets nuclear DNA. Images were obtained using a Leica AM TIRF MC microscope (Germany).

2.4. Statistical analysis

The results were used to determine their statistical significance. The statistical analysis of viability data was performed for $p < 0.05$ using GraphPad Prism 8.0.1 software (GraphPad, Boston, MA, USA). Two-way ANOVA with Tukey's multiple comparisons was applied as necessary. Statistical significance was assessed by analyzing the p-values. A p-value below 0.05 was marked statistically significant. If the p-value fell between 0.01 and 0.05, it was marked with an "*".

3. Results and discussion

3.1. Morphology analysis

It is evident from Fig. 1 that fibers reveal a uniform morphology without bead formation in all scaffolds. Increasing the collector rotational speed reduces the fiber diameter in both pure samples and those with the addition of nHA. This reduction is from the average diameter of 125 ± 32 nm for pure PLLA_R and 123 ± 9 nm for PLLA/nHA_R at low collector rotation speed (100 rpm) to the value of 111 ± 7 nm for PLLA_A and 110 ± 6 nm for PLLA/nHA_A at higher collector rotation speed (2000 rpm). Based on the results, the inclusion of nHA does not cause changes in the average fiber diameter. This is consistent with previous literature, which suggests that the addition of hydroxyapatite does not affect fiber diameter (e.g., (Van Manen et al., 2014)). SEM images reveal a uniform distribution of nHA nanoparticles within the fibers without any visible agglomerations (see Fig. 1 C, D).

Fig. 2 shows that increasing the collector rotational speed improves the fiber orientation, leading to an orientation with a narrow distribution for fibers collected at 2000 rpm, contrary to randomly arranged fibers collected at 200 rpm. The fiber orientation distribution's full width at half maximum (FWHM) decreases from 87.90 at 100 rpm to 22.40 at 2000 rpm for both pure and doped PLLA. Higher rotational speeds increase tensile forces, enhancing the fibers' stretching and alignment (Obregon et al., 2016). The anisotropy index (α) confirms this tendency. As the rotational speed increased from 100 to 2000 rpm, the α value increased from 0.27 to 0.91 for pure PLLA and from 0.33 to 0.89 for PLLA with the addition of nHA. These results indicate an increase in the orientation of nanofibers with increasing collector rotation speed and no effect of the addition of nHA on the anisotropy index.

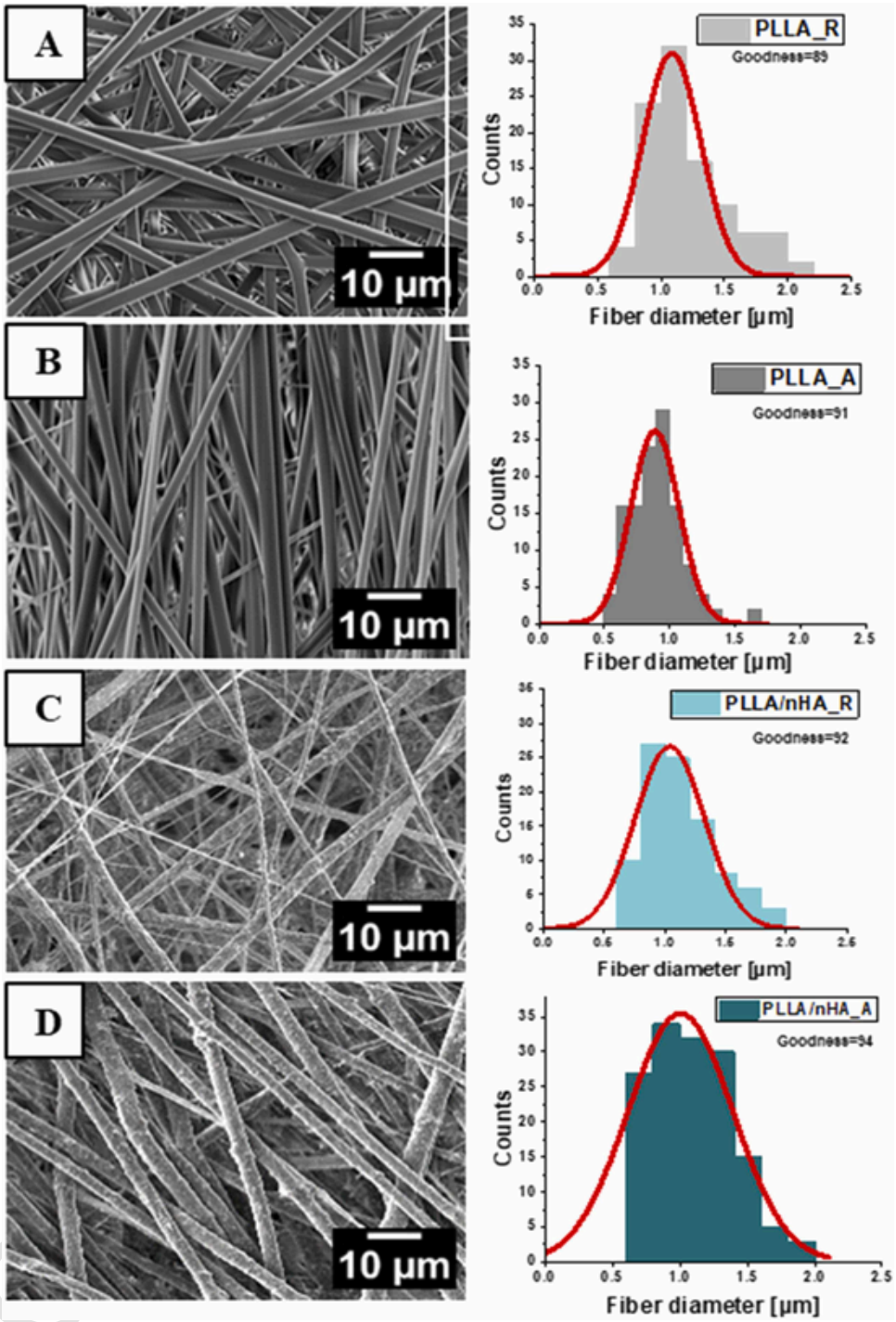

Fig. 1. SEM micrographs of A) PLLA_R, B) PLLA_A, C) PLLA/nHA_R, and D) PLLA/nHA_A nanofibrous scaffolds with corresponding diameter distributions approximated with Gaussian function.

The analysis of porosity and mean pore size clearly indicates the effect of nHA addition. It leads to higher porosity of nonwovens and slightly lower pore size. In the case of PLLA_R samples, addition of nHA results in an increase of porosity from 82 ± 0.4 % to 89 ± 1.1 %, and for PLLA_A nonwovens from 85 ± 1.2 % to 94 ± 0.6 %. The mean pore size was reduced, irrespective of the fibers alignment from ~202 ± 6 nm to ~194 ± 9 nm after nHA addition. The effect of fiber alignment is negligible. Porosity is an important factor in tissue engineering because it allows better penetration of nutrients and gases and promotes angiogenesis (Buitrago-Vásquez and Ossa-Orozco, 2018).

Verification of the presence of hydroxyapatite nanoparticles is shown in Table 1. Using the EsB detector, material contrasts were observed, which enabled the differentiation of individual components within the sample structure based on differences in the grayscale. In the case of doped samples, EDS analysis revealed the presence of key chemical elements characteristic of nHA nanoparticles, such as calcium (Ca) and phosphorus (P), in addition to the basic PLLA elements- carbon (C)

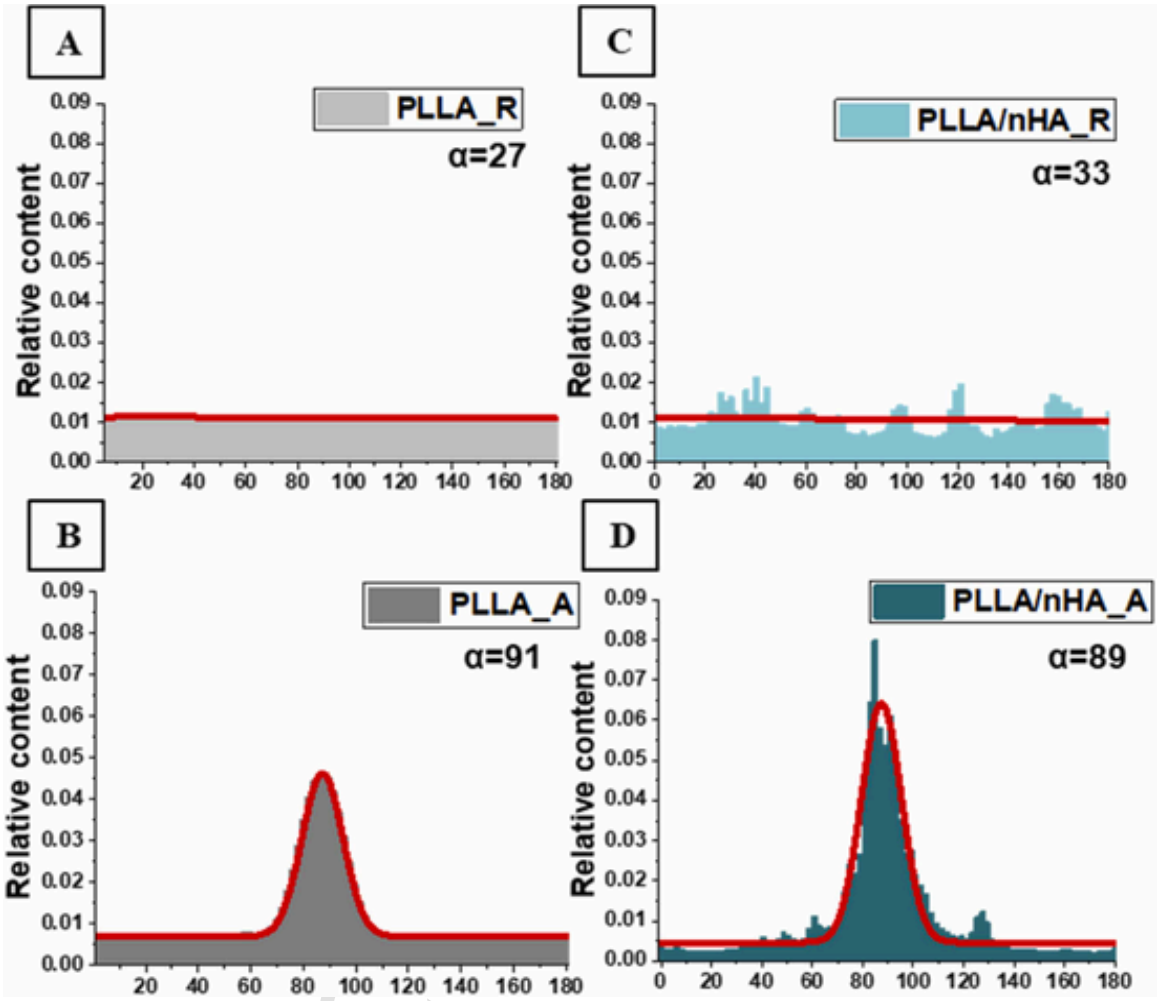

Fig. 2. Orientation distributions approximated with Gaussian function of all samples with anisotropy index α calculated from Eqs. (1) and (2) for samples A) PLLA_R, B) PLLA_A, C) PLLA/nHA_A and D) PLLA/nHA_A.

Table 1
PLLA scaffold elemental composition in wt% as measured using SEM-EDS.

Element	PLLA_R	PLLA_A	PLLA/nHA_R	PLLA/nHA_A
C	61.81 ± 0.7	61.97 ± 0.6	60.47 ± 0.3	60.13 ± 0.4
O	38.19 ± 0.3	38.03 ± 0.4	33.9 ± 0.7	33.81 ± 0.6
Ca	-	-	3.52 ± 0.4	3.79 ± 0.3
P	-	-	2.11 ± 0.2	2.27 ± 0.1
Other	-	-	-	-

and oxygen (O). This confirms that the hydroxyapatite nanoparticles were successfully added to the PLLA structure.

3.2. Water contact angle measurements, surface free energy, and water uptake determination

Fig. 3 shows the contact angle measurements, while Table 2 shows the SFEs and their components for all electrospun scaffolds. It is evident from Fig. 3 that the contact angles measured by using formamide are much lower compared with water and diiodomethane. Comparison of wettability within each group of fiber topography (random and aligned) clearly indicates the reduction of contact angle by addition of nHA being observed in all liquids. The effect of fiber arrangement on wettability is negligibly small if any. It is known from the literature that the wettability is strongly correlated with roughness which in

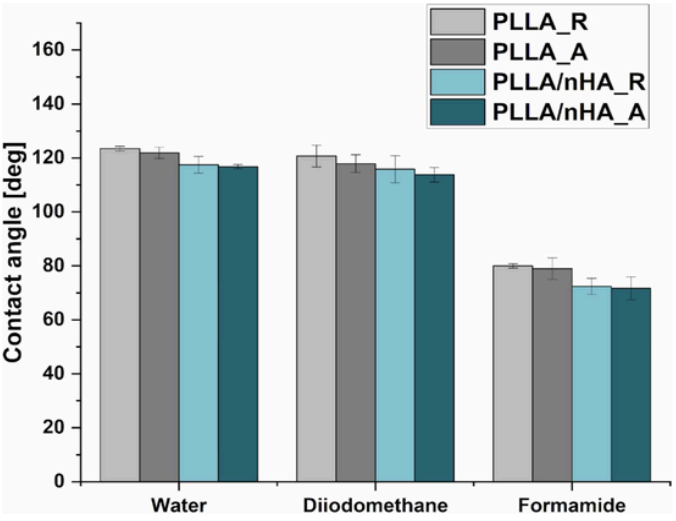

Fig. 3. Contact angle measurements for all electrospun scaffolds.

Table 2
SFE, water contact angle (WCA), and their components for all nanofibrous scaffolds.

Sample ID	Water Contact Angle [°]	Dispersive Component [mN/m]	Polar component [mN/m]	Surface Free Energy [mN/m]	Surface Polarity [Xp]	Water Uptake [%]
PLLA_R	123 ± 0.3	27.3 ± 2.1	2.7 ± 0.4	30 ± 2.2	0.0989	140 ± 2
PLLA_A	121.7 ± 0.4	29 ± 2.1	4.1 ± 0.6	33.1 ± 0.3	0.1413	149 ± 5
PLLA/nHA_R	117 ± 0.3	29.8 ± 0.4	3.6 ± 0.5	33.4 ± 0.9	0.1208	215 ± 7
PLLA/nHA_A	116 ± 0.2	34.5 ± 1.1	8.4 ± 0.3	42.9 ± 1.1	0.2434	257 ± 4

turns depends on fibers arrangement, being higher for randomly arranged fibers (Szewczyk et al., 2019). Therefore, it can not be excluded that the slightly higher contact angle for randomly arranged fibers is at least partly due to the more rough surface of random nonwovens. The reduction in contact angle by nHA addition is important for cell adhesion to the nanofiber surface, which is beneficial in tissue engineering applications (Paragkumar N et al., 2006).

The SFE analysis reveals that aligned samples generally exhibit higher values (see Table 2), with SFE measured at 30 ± 2.2 mN/m and 33.4 ± 0.9 mN/m for random PLLA and PLLA/nHA, respectively, compared to 33.1 ± 0.3 mN/m for aligned PLLA, and 42.9 ± 1.9 for aligned PLLA with nHA addition. The ascending order of SFE is PLLA_R > PLLA_A > PLLA/nHA_R > PLLA/nHA_A. The Kaelble-Owens-Wendt method was used to calculate the total SFE, which combines the polar component resulting from hydrogen bonds and dipole-dipole interactions with the dispersive component resulting from London and van der Waals forces (Rudawska and Jacniacka, 2009). Notably, the dispersion component was the main factor influencing the SFE of PLLA substrates. Moreover, the dispersion component showed an increasing trend in the following order: PLLA_R > PLLA_A > PLLA/nHA_R > PLLA/nHA_A.

PLLA_R indicated a lower polar component of the contact angle than PLLA_A. Therefore, the surface polarity (*Xp*) of PLLA_A was higher than PLLA_R. Additionally, polar components increased with the nHA additive, which was more effective for aligned fibers. Weak crystallinity and molecular order decide lower surface polarity (Kołbuk et al., 2022; Zaszczyńska et al., 2024b; Vijayendran, 1979), which was observed for PLLA_R. Adding nHA increases the surface polarity of PLLA/nHA_R and PLLA/nHA_A due to its low polar component γ_{sp} equal to c.a. 16.4 mN/m and related low WCA (Nasker et al., 2019). Surface polarity enhances protein adsorption, which was confirmed by using fibronectin (Barroca et al., 2018). From Fig. 4, it is evident that the highest water uptake was in samples with nHA addition. The PLLA/nHA aligned scaffold showed a lower percentage of water absorbed at the first minute. Still, it gradually increased till the second minute. The results showed that PLLA/nHA in random and aligned scaffolds exhibit better hydrophilicity than pure PLLA random or PLLA_A scaffolds. Also, it exhibits increased water uptake due to the hydrophilicity of nHA and its ionic exchange with water. According to the literature, this ionic exchange with the surrounding medium results in degradation and the formation of microporosities that enhance water uptake (Buitrago-Vásquez and Ossa-Orozco, 2018). Both the material's initial porosity and the fibers' porosity caused by nHA dissolution may play a significant role in water uptake. In summary, adding nHA increased samples' SFE and water uptake and is very important for porous materials dedicated to tissue engineering applications (Bhat et al., 2013).

3.3. Fourier transform infrared spectroscopy (FTIR)

FTIR spectra of all investigated electrospun fibers as well as PLLA before electrospinning (powder) and pure hydroxyapatite, are presented in Fig. 5. The main peaks of PLLA and nHA are summarized in Table 3 and assigned to the particular vibration data.

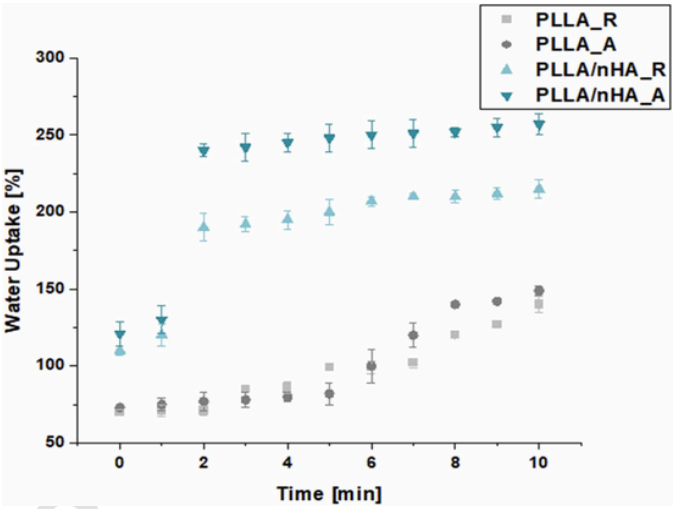

Fig. 4. Water uptake of the four kinds of scaffolds in deionized water over time calculated from Eq. (8).

FTIR spectra of pure PLLA fibers formed at low and high rotational collector speed, do not show any differences. What is important is that there is no peak at 921 cm^{-1}, which is usually assigned to the crystalline form of PLLA, indicating that the samples do not contain crystals (Hambleton and Mele, 2024; Polak et al., 2023). The analysis of FTIR spectra of PLLA/nHA samples indicates the existence of all peaks related to PLLA and nHA. This observation leads to the conclusion that nHA is effectively loaded into PLLA fibers. Considering the partial overlapping of some of the PLLA and nHA peaks, we could not estimate the content of nHA in PLLA/nHA fibers. Additionally, there is no essential shift in the positions of the peaks of PLLA and nHA in PLLA/nHA fibers, indicating no molecular interactions between both components.

3.4. Wide angle X-ray scattering (WAXS)

Fig. 6 illustrates WAXS profiles for all fibers. It is evident after subtraction of the nHA profile of crystalline nature that all spun PLLA

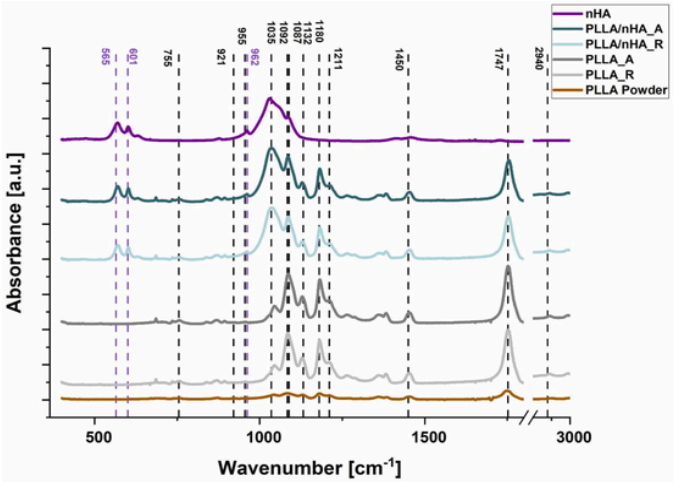

Fig. 5. FTIR spectra of hydroxyapatite particles, PLLA powder, electrospun pure PLLA, and PLLA/nHA scaffolds with random and aligned fiber orientation.

Table 3
Experimentally observed main FTIR peaks of PLLA and nHA.

Sample	Abbreviation	Vibrational mode	Position [cm^{-1}]	Ref.
nHA	ν_β PO_4	PO_4 bending (ν_β)	1092	(Stoch et al., 2000; Lopresti et al., 2020; Panda et al., 2022)
	ν_1PO_4	PO_4 stretching (ν_1)	962	(Panda et al., 2022)
	ν_4PO_4	PO_4 bending (ν_4)	601 555	
PLLA	ν(C-COO)	Stretching C-COO	868	(Leroy et al., 2017)
	ν_s(C-CH_3)	Symmetrical stretching C-CH_3	1035	(Leroy et al., 2017)
	ν_s(C-O-C)	Symmetrical stretching C-O-C	1092	(Pariy et al., 2022)
	ν_{as} (C-O) + τ (CH_3)	Symmetrical stretching and twisting	1180, 1211	(Pariy et al., 2022)
	δ_{as}(CH_3)	Asymmetrical scissoring	1450	(Scaffaro et al., 2023)
	ν(C═O)	Stretching	1747	(Scaffaro et al., 2017)
	ν(CH_2)	Symmetrical stretching	2940	(Nazir et al., 2021; Ribeiro et al., 2011)

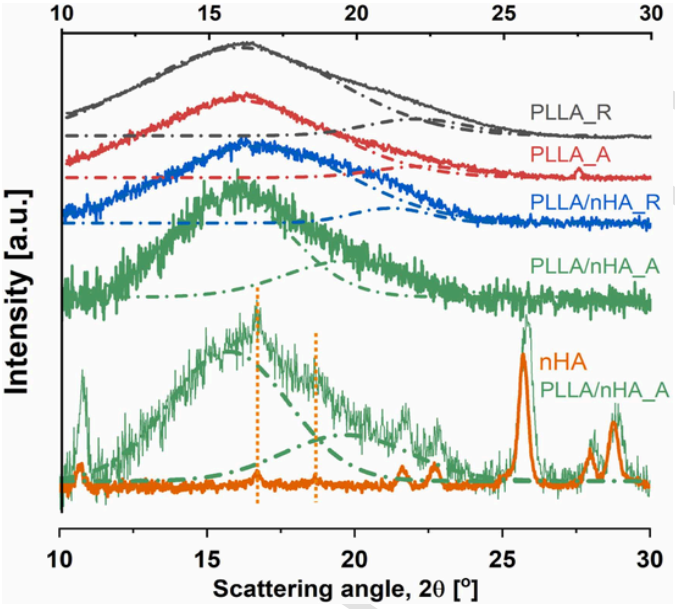

Fig. 6. WAXS profiles of analyzed fiber mats.The profiles at the bottom show a nHA profile, and the original profiles for the fibers doped with nHA display the nHA diffraction peaks; the upper curves show these profiles after subtraction of the nHA diffraction peaks, which were approximated with Gaussian function during peak deconvolution. For clarity, the upper profiles were shifted vertically. The vertical orange dashed lines indicate the positions of the most intense diffraction peaks of the α'phase of PLLA (Pan et al., 2007; Righetti et al., 2015), which overlap the small nHA diffraction peaks. Peak deconvolution of the asymmetric halo required two Gaussian function peaks.

and PLLA doped with nHA fibers, both random and aligned, are amorphous. However, it is evident that the shape of the amorphous profile is not unimodal, requiring the approximation use of two Gaussian functions. This fact indicates that the amorphous structure in spun PLLA fibers is not completely disordered. It has two local maxima, indicated by peak deconvolution requiring two Gaussian peaks, suggesting the existence of some ordering with two most probable interatomic distances.

3.5. Differential scanning calorimetry (DSC)

The curves in Fig. 7 represent the apparent heat capacity, C_p, normalized to PLLA mass, which were determined from the DSC heating scans registered at 10 K/min for as spun fibers. All the samples, which at ambient conditions are amorphous (as indicated by WAXS analysis), show several transitions during heating. Generally, we see qualitatively similar behavior: below 50 ºC, there is a linear increase in C_p with temperature. Between 50 ºC and 80 ºC there are two sharp thermal effects, where the endothermic one is seen to change abruptly into the exothermic one. Between 80 and 150 ºC there is an additional broad exothermic effect. Above 160 ºC starts a strong endothermic effect with a maximum at c.a. 180–190 ºC. Above 200 ºC there is a linear increase in C_p with temperature.

For pure PLLA fibers, the linear trend below 50 ºC agrees with the behavior of PLLA Cp below the glass transition temperature, T_g, and reflects the C_p temperature dependence of PLLA at the glassy/crystal state (C). Above 200 ºC, the linear trend agrees with the Cp behavior of PLLA in an amorphous state (A) (Pyda and Czerniecka-Kubicka, 2017). The respective lines for C_p(C) and C_p(A) were plotted as dash-dotted lines in Fig. 12 for reference.

The PLLA glass transition temperature, T_g, is expected at 59 ºC (Pyda and Czerniecka-Kubicka, 2017). However, in this temperature range, we observe the abrupt sharp endothermic and exothermic effects, which cover the expected C_p change, ΔC_p, at T_g, making its determination difficult. The sharp endothermic effect at 55 ºC is interpreted as an enthalpy relaxation (Pyda and Czerniecka-Kubicka, 2017), which is typical for PLLA and is known to depend on the thermal history. The sharp exothermic effect at 70 ºC reflects crystallization from the glassy state (referred to as cold crystallization, cc), which is typically observed during heating for samples with reasonably high content of the mobile amorphous phase. However, it has to be noted that the temperature position and shape of the cc peak does not resemble the results found in the literature (Pyda and Czerniecka-Kubicka, 2017) for amorphous samples cooled from the melt. It is highly probable that this fast cold crystallization occurs in a highly disordered α' phase, as indicated by WAXS analysis.

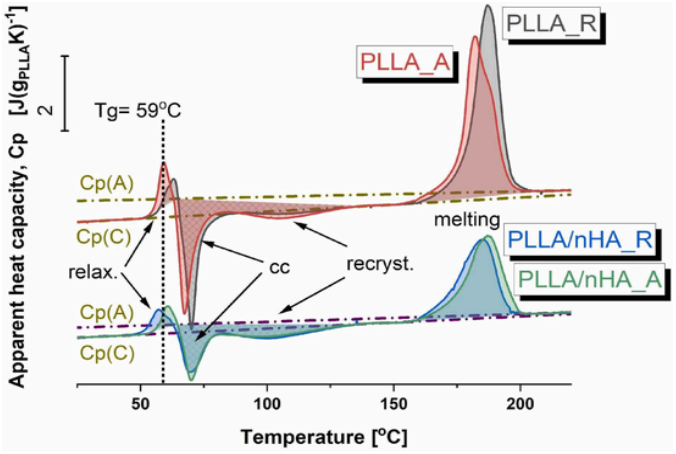

Fig. 7. Apparent heat capacity determined during 1st heating at 10 K/min for as-spun fibers. The curves for pure PLLA and doped with nHA are shifted along the y axis for clarity, and the scale bar is given. The exothermic effects of cc and recrystallization are indicated with grid-shaded areas; the endothermic enthalpy relaxation and melting are indicated with shaded areas. The linear approximation of temperature dependence of the heat capacity for amorphous and crystalline states (C_p(A), C_p(C)) determined by us are plotted as dash-dotted lines. The glass transition temperature, T_g, is indicated after (Pyda and Czerniecka-Kubicka, 2017).

The additional broad exothermic effect observed between 80 and 150 ºC also does not resemble typical thermal effects reported in the literature for bulk PLLA samples cooled from melt and crystalizing during heating from the glassy state. However, it must be related to further recrystallization and/or polymorphic crystal-crystal transition (Di Lorenzo and Androsch, 2019). Assuming our hypothesis that the cold crystallization results in the formation of the α' phase, it is highly probable that transitions in the temperature range between 80 and 160 ºC contain α'- α transition. This effect is followed by the final endothermic melting peak at c.a. 180–190 ºC, similar to the results in the literature.

A comparison of the curves in Fig. 7 shows that the thermal effects for the fibers doped with nHA are much smaller than for pure PLLA fibers. Moreover, for fibers doped with nHA, the PLLA heat capacity in an amorphous state, C_p(A) at T > 200 ºC, was lower than for pure PLLA fibers.

The enthalpies of the thermal effects observed during heating: relaxation, cold crystallization/recrystallization, and melting, are presented in Fig. 8. Enthalpy relaxation is seen as the strongest for aligned pure PLLA fibers (c.a. 5 J/g_{PLLA}) as compared to other samples (c.a. 3 J/g_{PLLA}). It indicates the highest orientation of the polymer chains and extended chain conformation in aligned pure PLLA fibers, which probably leads to higher crystallization enthalpy during further heating (c.a. 38 J/g_{PLLA}). It is, however, not reflected in the melting enthalpy, as the highest value is observed for pure random PLLA fibers (c.a. 65 J/g_{PLLA}), which corresponds to c.a. 71 % of crystallinity. This may be related to differences in polymorphic phase content indicated by a single melting peak for PLLA_R and a double melting peak for PLLA_A (Fig. 8).

For PLLA doped with nHA, we see much lower crystallization and melting enthalpies than for pure PLLA fibers (ΔHc = 25 and ΔHm = 36 J/g_{PLLA}, respectively), indicating 40 % crystallinity developed during heating. The collector rotational speed has no apparent effect on the PLLA/nHA fibers. It is clear that nHA reduces the crystallization ability of PLLA, most probably by affecting the polymer chain mobility as indicated by the lower heat capacity of the nHA doped vs pure PLLA samples.

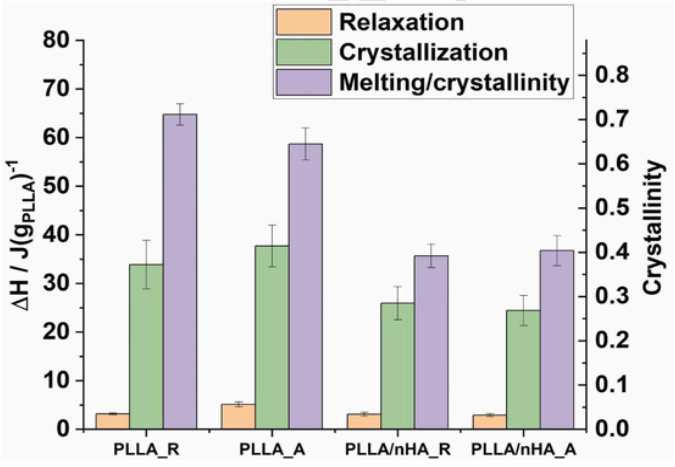

Fig. 8. The enthalpies of the thermal effects observed during the 1st heating scans are seen in Fig. 7 for enthalpy relaxation, cold crystallization/recrystallization, and melting. The right y scale indicates the crystallinity, which appeared during the 1st heating, calculated from the melting enthalpy, using the value of heat of fusion for the 100 % crystalline sample, Δh_m^0 = 91 J/g (Pyda and Czerniecka-Kubicka, 2017).

3.6. Piezoelectric coefficient measurements

Piezoelectric coefficient measurements on fibers were carried out to examine how rotation speed and the addition of nHA affect the piezoelectric properties of prepared materials, see Fig. 9.

The results reveal significant differences in the piezoelectric coefficients between samples subjected to different collector rotation speeds. Specifically, PLLA_A exhibits a notably higher piezoelectric coefficient (4.58 ± 0.08 pCN^{-1}) than PLLA_R (4.04 ± 0.21 pCN^{-1}). This suggests that the increased rotation speed of the collector results in higher piezoelectric properties of the PLLA-based materials. Moreover, introducing hydroxyapatite nHA nanoparticles into the PLLA matrix influences the piezoelectric coefficient. PLLA/nHA_R and PLLA/nHA_A exhibit slightly higher coefficients (4.42 ± 0.13 pCN^{-1} and 4.68 ± 0.08 pCN^{-1}, respectively) than their non-nHA counterparts. Comparing the samples, PLLA/nHA_A demonstrates the highest piezoelectric coefficient, suggesting that the combination of higher collector rotation speed and nHA nanoparticles yields the most favorable piezoelectric response.

It is anticipated that the higher rotation rate forces a stretching of polymer chains. Although the polymer remains practically amorphous, with some traces of precrystalline local ordering (WAXS data), there is a change in molecular conformation, increasing polarization and piezoelectricity (Polak et al., 2023).

As for the PLLA with hydroxyapatite, our structure analysis results indicate that the increase of piezoelectric coefficient over the value of pure PLLA is most probably due to the contribution of higher nHA piezoelectricity compared to PLLA, only. The calculated piezoelectric coefficient for hexagonal phase d_{33} ~6.4 pm/V is consistent with the previously obtained value for monoclinic nHA (15.7 pm/V) (Polak et al., 2023).

3.7. In vitro study

Osteoblasts are fundamental for continuous bone remodeling and play an important role in evaluating materials for bone tissue engineering (Zhu et al., 2021a). Therefore, parallel to cellular viability, we determined osteoblasts nonwovens interaction.

Cell viability was assessed for MG-63 cultured on pure PLLA scaffolds and with the nHA addition, with random and aligned fiber orientation (Fig. 10). The in vitro analysis confirmed the non-toxic properties of all PLLA nanofibrous scaffolds. All scaffolds reached ≥ 70 % values of viability, which is in accordance with the ISO 10993–5 standard con-

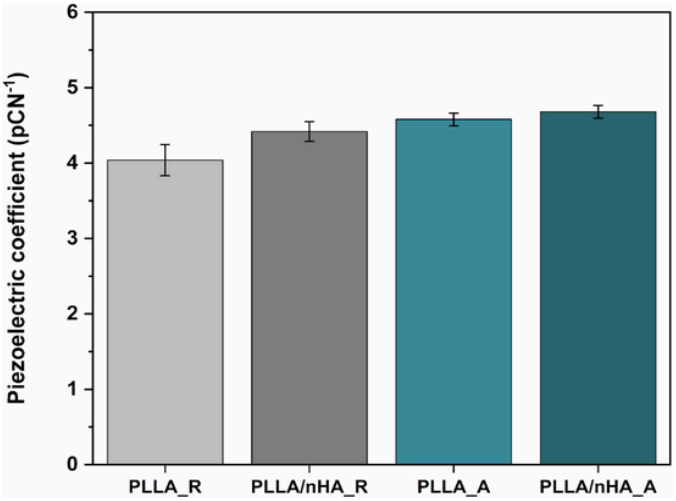

Fig. 9. Results from d_{33} piezoelectric coefficient measurement.

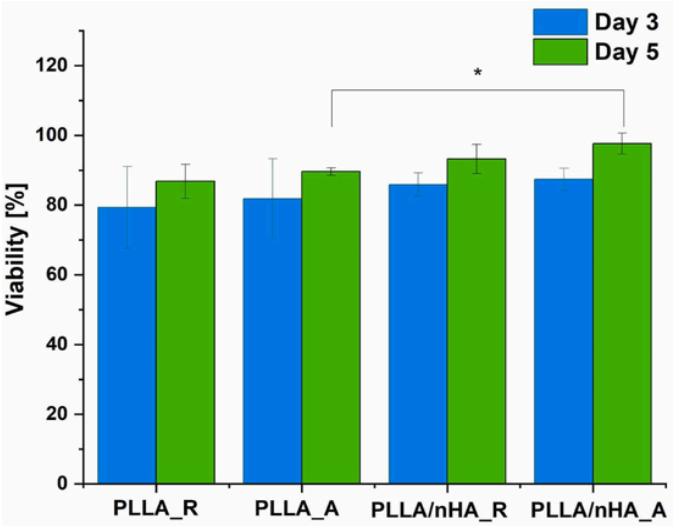

Fig. 10. Cell viability of MG-63 cells cultured on pristine and with nHA addition PLLA nanofibrous scaffolds as the rate of TCP (Tissue Culture Plastic, 100 %). Statistical significance: * $p < 0.05$.

nected to the nontoxic materials for cells. Cell proliferation and attachment represent the initial stages of tissue regeneration and are essential for tissue regeneration (Jeznach et al., 2022). Hence, an assessment of cellular morphology was conducted. Following 3 and 5 days of cell cultivation directly seeded onto pristine PLLA scaffolds and PLLA/nHa, immunostained cells were analyzed using fluorescence microscopy (See Figs. 11 and 12). The morphology and spreading of osteoblasts in contact with the sample's surface closely resembled those observed on TCP, indicating cellular viability. The cells displayed well-spread morphology and demonstrated robust intercellular interactions. Effective osteoblasts-nonwoven interaction was confirmed by the elongation of cells, and notably, cell spreading was particularly pronounced on PLLA/nHA_A composite nanofibers. On aligned fibers cells align themselves and grow along the fibers more than they do on random meshes where they spread to a more round shapes. Previous studies have underscored the importance of integrating nanoscale components like nHA into engineered scaffolds to promote cell proliferation (Amarjargal et al., 2019). Consequently, the enhanced adhesion and proliferation of PLLA/nHA fibers can be attributed to the inclusion of nHA nanoparticles, which is related to reduced hydrophobicity (Table 2). An *in vitro* study substantiates that the PLLA/nHA nanofibrous scaffold exhibits increased bioactivity and holds promise for stimulating bone formation (Softas, 2022).

4. Discussion

In recent years, the growing demand for bone substitutes in clinical settings has fueled advances in bone tissue engineering (Koons et al., 2020). A major goal in this field is the replication of the bone extracellular matrix (ECM). In these efforts, the integration of bioceramic materials with biocompatible scaffolds has gained much interest (Salerno and Netti, 2023). Although PLLA scaffolds have properties similar to bone (ECM, their application in tissue engineering is hampered by inherent limitations (Capuana et al., 2022). In response to these limitations, in this paper, a piezoelectric cell scaffold composed of PLLA/nHA was spun as smart scaffolds dedicated to tissue engineering.

The fiber alignment in piezoelectric scaffolds is crucial in scaffold implantation material-cell response and plays a significant role in determining the final properties of the scaffolds. In our results, two types of fiber arrangements were produced: random and aligned. In randomly arranged fiber scaffolds, the fibers create a porous and complex structure, which is beneficial for cell adhesion and nutrient diffusion. The random arrangement of fibers can promote the formation of a more natural, complex spatial network that supports tissue growth in different directions (Tamayol et al., 2013). In contrast, oriented fibers are produced by increasing the collector speed during electrospinning (in our article, increasing from 100 rpm to 2000 rpm). The aligned fibers and the addition of nHA to the structure of nanofibrous scaffolds increased the SFE and water uptake of the samples, which are important for porous materials intended for tissue engineering applications (Bhat et al., 2013). The alignment of the fibers *per se* increased the effective contact area, which led to slightly greater SFE. The fiber orientation promotes the formation of structures that are more similar to natural tissue structures, leading to better tissue integration and regeneration (Fernandez-Yague et al., 2015).

The results of wettability measurements indicate hydrophilization of the nonwovens by adding nHA. This tendency is reflected by surface free energy measurements, particularly evident for the aligned fibers geometry (SFE determined with the Kaelble-Owens-Wendt method 42.9 mN/m for PLLA/nHA versus 33.1 mN/m for pure PLLA). The effect of nHA is not so evident in the case this type of random structures (SFE 33.4 mN/m vs. 30 mN/m for PLLA/nHA and PLLA nonwovens, respectively). for which the surface is more roughly with possible air bubbles trapped between the fibers, resulting in additional wettability deviation.

One of the reasons for an increase in piezoelectric response in samples formed with higher collector rotational speed can be attributed to fiber alignment.When the fibers are aligned, the piezoelectric dipoles are oriented in a uniform direction, even in practically amorphous material, resulting in a more efficient conversion of mechanical stress into electrical signals. This alignment may better mimic the anisotropic nature of natural bone tissue, potentially leading to improved tissue regeneration outcomes. Additionally, the increase in the piezoelectric coefficient d_{33} is caused by the higher fiber arrangement and uniform distribution of nHA nanoparticles in the PLLA matrix. These nanoparticles act as nucleating agents, leading to the ordering of PLLA chains (Zhang et al., 2023b). This structural ordering is key to enhancing the piezoelectric effect because it provides a more efficient conversion of mechanical stress into electrical signals (Zhao et al., 2023). Comparing the piezoelectric coefficients d_{33} for randomly arranged and aligned PLLA nanofibers with the literature data, significant differences are visible, which reflect the influence of fiber orientation on their piezoelectric properties. In the literature, d_{33} values for random PLLA nanofibers are usually lower because the orientation of molecular dipoles is random, which leads to a reduction of the total piezoelectric effect. Typical d_{33} values for randomly arranged PLLA nanofibers range from about 1–3 pCN^{-1} (Zhao et al., 2017), while in our studies a value of 4.04 ± 0.21 pCN^{-1} was obtained. For aligned PLLA fibers, where the fibers are regularly aranged in one direction, the d_{33} coefficient increases significantly to 4.58 pCN^{-1} and is higher than that obtained in the literature (Ren et al., 2024). The development of composite scaffolds with increased piezoelectric properties opens new possibilities in the field of bone and nervous tissue engineering (Li, 2019). The observed improvements in piezoelectricity are particularly noteworthy because they play a key role in mimicking the natural electrical environment of bone tissue, thereby promoting cellular activities necessary for tissue regeneration (Kapat et al., 2020).

Our *in vitro* studies are important due to the development of new scaffolds that improve osteoblast proliferation thanks to the addition of nHA. Confirmation of this can be found in FTIR-ATR spectral analysis, where characteristic nHA peaks were detected, confirming the successful modification of PLLA fibers. Our findings support the effective integration of nHA with PLLA, leading to increased proliferation of MG-63 cells on nHA-supplemented scaffolds compared to basic PLLA scaffolds. This highlights the potential of these advanced scaffolds in bone tissue

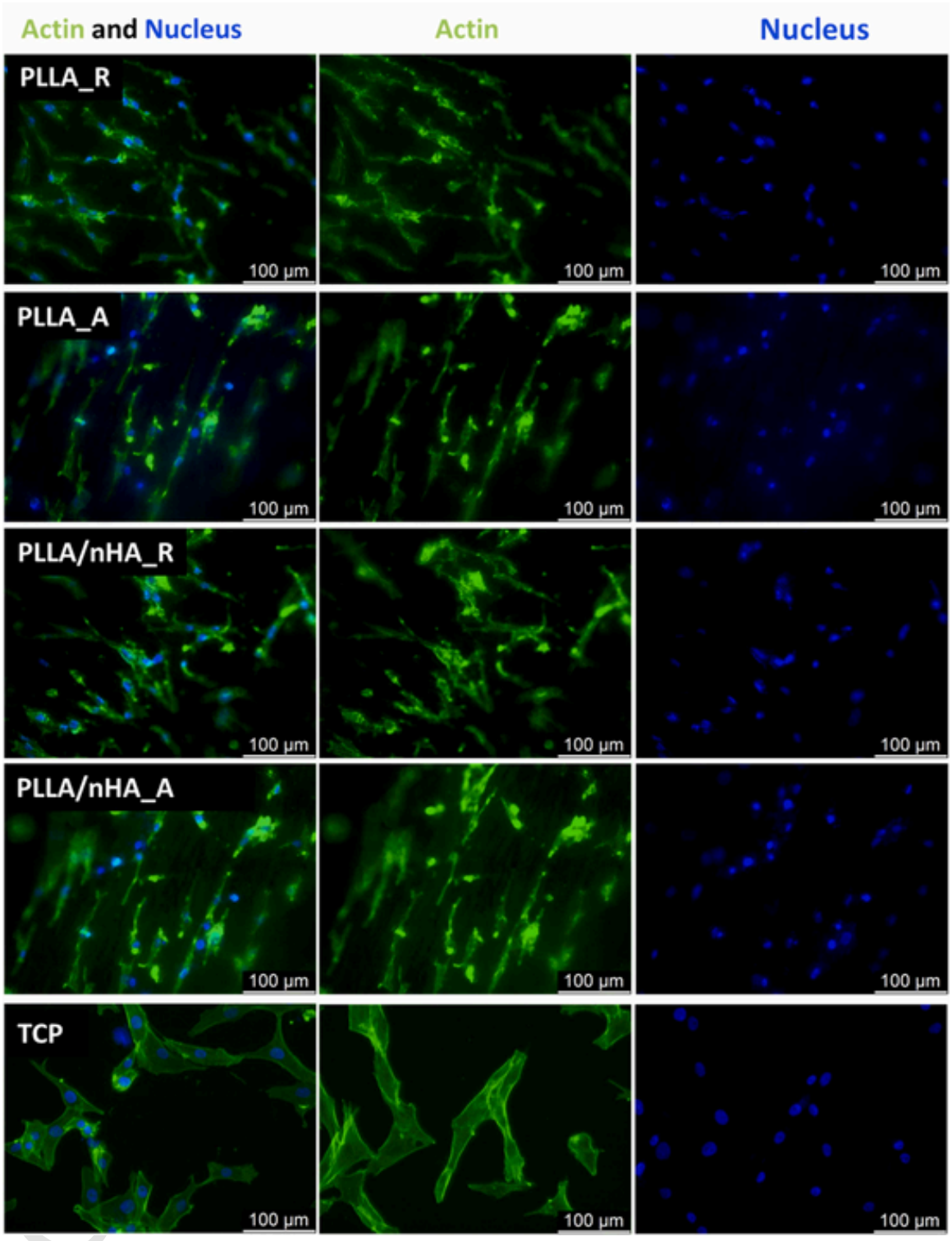

Fig. 11. FM images of MG-63 after immunofluorescent staining directly cultured on the nanofibrous scaffold for 3 days. Samples PLLA_R, PLLA_A, PLLA/nHA_R, and PLLA/nHA_A in comparison to TCP.

engineering. Additionally, Yanagida's (Yanagida et al., 2009) research on PLLA coated with HAp nanocrystals showed promising properties of implant materials, such as reduced inflammation and improved cell adhesion, suggesting the possibility of creating soft tissue-compatible and biodegradable scaffolds. Similarly, Liao's work (Liao et al., 2006) on biodegradable PLLA/nHA/collagen composites highlighted increased neutrophil responsiveness, highlighting the need for further *in vivo* studies on the effectiveness of scaffolds in critical bone regeneration. These collaborative discoveries contribute to a better understanding of the potential applications of innovative biomimetic materials in tissue engineering. The initiation of osteogenesis in the presence of nHA coating on PLLA is complex and involves various factors such as biomineral-

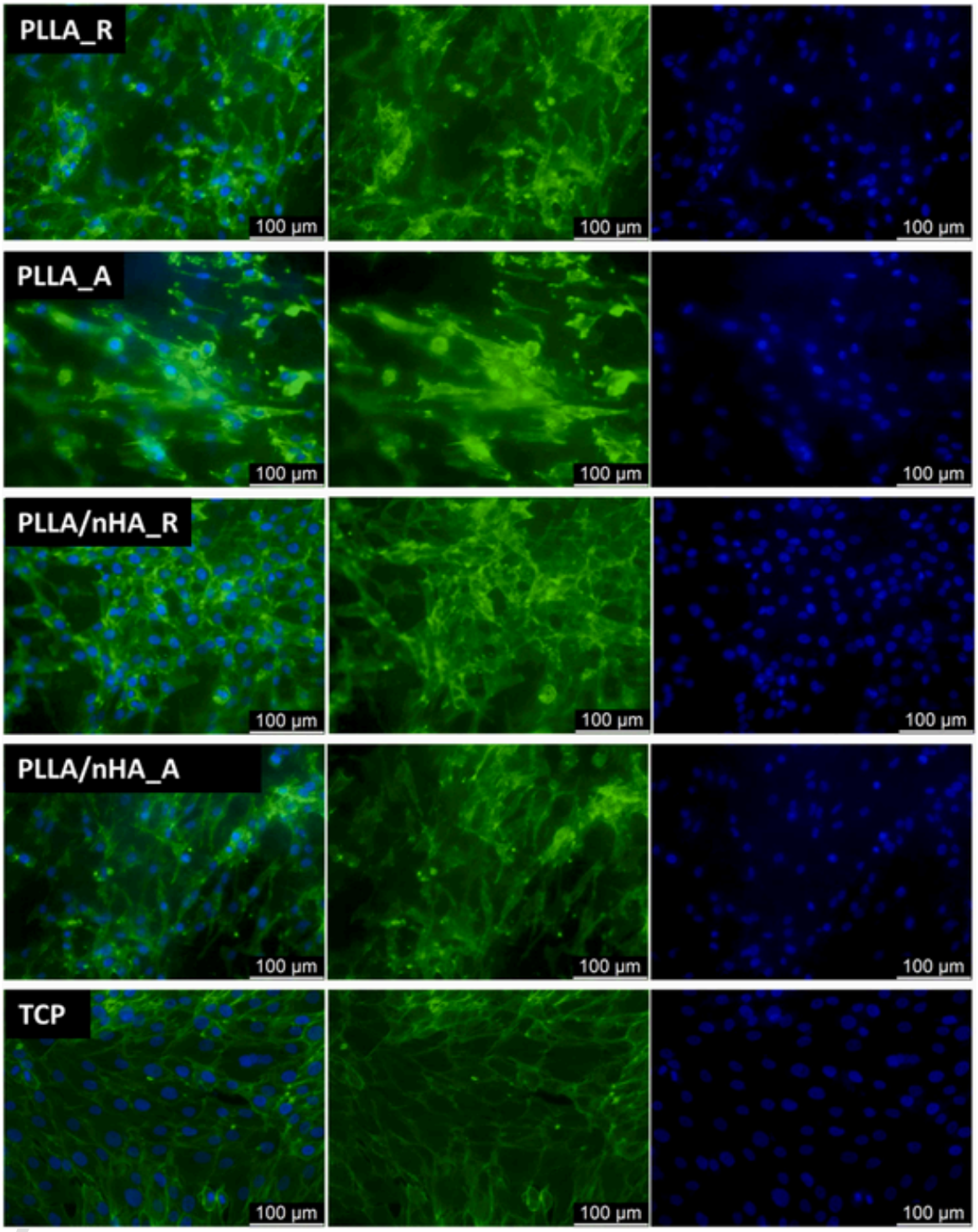

Fig. 12. FM images of MG-63 after immunofluorescent staining directly cultured on the nanofibrous scaffold for 5 days. Samples PLLA_R, PLLA_A, PLLA/nHA_R, and PLLA/nHA_A in comparison to TCP.

ization, osteoconductive properties, signals transmission, and optimized cell-material interactions. We note that nHA promotes the deposition of nHA crystals, mimicking natural mineralization (Ielo et al., 2022). Additionally, its osteoconductive properties support the adhesion and migration of osteogenic cells (Zhu et al., 2021b), and the release of ions from nHA acts as important signals to catalyze osteogenic differentiation (Armiento et al., 2020).

5. Conclusions

The goal of this work was to develop an electrospun nanofibrous scaffold with PLLA and evaluate the effects of nHA addition on its properties for bone tissue engineering applications. The influence of changing the collector rotational speed on the properties of the scaffolds was determined. The electrospinning process was successful, and homogenous fibers were obtained with and without adding nHA. The presence

of nHA showed no significant impact on the morphology of the fibers and their alignment for different rotational speeds. FTIR spectroscopy did not present any important changes in composition nor detect any interaction between constituents.

The hydrophilization of the nonwovens by adding nHA is clearly visible, being particularly evident for the aligned fibers geometry WAXS results show that all the fibers are in an amorphous state indicated by a lack of diffraction peaks. However, the presence of some disordered α' phase may be inferred from the asymmetric shape of the amorphous halo. DSC analysis revealed the presence of intense enthalpy relaxation effects at the glass transition temperature, the largest being for pure aligned PLLA fibers. All samples, being in the non-equilibrium (non-relaxed) amorphous/disordered α' phase state, intensively crystallize at temperatures just above T_g and recrystallize during further heating, developing much higher crystallinity for pure PLLA than for doped with nHA, 70 % vs 40 %, respectively. Additionally, PLLA/nHA fibers show lower heat capacity for PLLA in an amorphous state, indicating that nHA reduces PLLA molecular mobility.

Furthermore, PLLA fibers loaded with nHA showed increased porosity by 7–9 % compared to their counterparts, which is beneficial for tissue engineering applications. Most importantly, the piezoelectric coefficient d_{33} was impacted by rotational speed and nHA presence. For the samples without nHA, obtained values were 4.04 pCN^{-1} for 100 rpm and 4.58 pCN^{-1} for 2000 rpm and increased further in its presence to 4.42 pCN^{-1} and 4.68 pCN^{-1}, respectively. Notably, our results show that the nHA can lead to the formation of more piezoelectric structure regardless of rotational speed. In addition, the nanoadditive improved osteoblast proliferation as reported by others.

The developed PLLA/nHA nanofibrous scaffold holds great promise for bone tissue engineering, offering biodegradability combined with reasonable piezoelectricity, porosity and slightly increased hydrophilicity due to nHA presence.

Ethical approval

Not applicable.

Uncited reference

Qin et al., (2024)

CRediT authorship contribution statement

Angelika Zaszczyńska: Writing – original draft, Visualization, Validation, Supervision, Software, Project administration, Methodology, Investigation, Formal analysis, Data curation, Conceptualization. **Dorota Kołbuk:** Writing – review & editing, Writing – original draft, Methodology, Investigation. **Arkadiusz Gradys:** Writing – review & editing, Writing – original draft, Supervision, Methodology, Investigation, Formal analysis, Conceptualization. **Konrad Zabielski:** Writing – review & editing, Writing – original draft, Methodology, Investigation. **Urszula Stachewicz:** Writing – review & editing, Writing – original draft, Supervision. **Piotr Szewczyk:** Writing – review & editing, Writing – original draft, Methodology, Investigation. **Paweł Sajkiewicz:** Writing – review & editing, Writing – original draft, Visualization, Validation, Supervision.

Declaration of Competing Interest

The authors declare that they have no known competing financial interests or personal relationships that could have appeared to influence the work reported in this paper.

Acknowledgments

The study was partially supported by the funding from the European Union's Horizon 2020 research and innovation programme under grant agreement No 958174, and within M-ERA.NET 3 funded by National Science Centre, Poland No 2021/03/Y/ST5/00231.

Data availability

Data will be made available on request.

Appendix A. Supporting information

Supplementary data associated with this article can be found in the online version at doi:10.1016/j.micron.2024.103743.

References

Amarjargal, A., Brunelli, M., Fortunato, G., Spano, F., Kim, C.S., Rossi, R.M., 2019. On-demand drug release from tailored blended electrospun nanofibers. J. Drug Deliv. Sci. Technol. 52, 8–14. https://doi.org/10.1016/j.jddst.2019.04.004.

Armiento, A.R., Hatt, L.P., Sanchez Rosenberg, G., Thompson, K., Stoddart, M.J., 2020. Functional biomaterials for bone regeneration: a lesson in complex biology. Adv. Funct. Mater. 30, 1909874. https://doi.org/10.1002/adfm.201909874.

Baniasadi, H., Madani, M., Seppälä, J., Zimmerman, J.B., Yazdani, M.R., 2023. Form-stable phase change electrospun nanofibers mat with thermal regulation and biomedical multi-functionalities. J. Energy Storage 68, 107660. https://doi.org/10.1016/j.est.2023.107660.

Barbosa, F., Garrudo, F.F.F., Alberte, P.S., Resina, L., Carvalho, M.S., Jain, A., Marques, A.C., Estrany, F., Rawson, F.J., Aléman, C., et al., 2023. Hydroxyapatite-filled osteoinductive and piezoelectric nanofibers for bone tissue engineering. Sci. Technol. Adv. Mater. 24, 2242242. https://doi.org/10.1080/14686996.2023.2242242.

Barroca, N., Marote, A., Vieira, S.I., Almeida, A., Fernandes, M.H.V., Vilarinho, P.M., Da Cruz E Silva, O.A.B., 2018. Electrically polarized PLLA nanofibers as neural tissue engineering scaffolds with improved neuritogenesis. Colloids Surf. B: Biointerfaces 167, 93–103. https://doi.org/10.1016/j.colsurfb.2018.03.050.

Bauso, L.V., La Fauci, V., Longo, C., Calabrese, G., 2024. Bone tissue engineering and nanotechnology: a promising combination for bone regeneration. Biology 13, 237. https://doi.org/10.3390/biology13040237.

Behroozi, A.H., Al-Shaeli, M., Vatanpour, V., 2023. Fabrication and modification of nanofiltration membranes by solution electrospinning technique: a review of influential factors and applications in water treatment. Desalination 558, 116638. https://doi.org/10.1016/j.desal.2023.116638.

Bhat, K.A., Leo Prakash, P., Manoharan, N., Lakshmibai, A., Sangeetha, D., 2013. Fabrication of polymethyl methacrylate/polysulfone/nanoceramic composites for orthopedic applications. J. Appl. Polym. Sci. 127, 2764–2775. https://doi.org/10.1002/app.37581.

Bose, S., Roy, M., Bandyopadhyay, A., 2012. Recent advances in bone tissue engineering scaffolds. Trends Biotechnol. 30, 546–554. https://doi.org/10.1016/j.tibtech.2012.07.005.

Bose, S., Sarkar, N., Jo, Y., 2024. Natural medicine delivery from 3D printed bone substitutes. J. Control. Release 365, 848–875. https://doi.org/10.1016/j.jconrel.2023.09.025.

Buitrago-Vásquez, M., Ossa-Orozco, C.P., 2018. Degradation, water uptake, injectability and mechanical strength of injectable bone substitutes composed of silk fibroin and hydroxyapatite nanorods. Rev. Fac. Ing. 27, 49–60. https://doi.org/10.19053/01211129.v27.n48.2018.8072.

Capuana, E., Lopresti, F., Ceraulo, M., La Carrubba, V., 2022. Poly-l-lactic acid (PLLA)-based biomaterials for regenerative medicine: a review on processing and applications. Polymers 14, 1153. https://doi.org/10.3390/polym14061153.

Cartier, L., Okihara, T., Ikada, Y., Tsuji, H., Puiggali, J., Lotz, B., 2000. Epitaxial crystallization and crystalline polymorphism of polylactides. Polymer 41, 8909–8919. https://doi.org/10.1016/S0032-3861(00)00234-2.

Chen, Y., Dong, X., Shafiq, M., Myles, G., Radacsi, N., Mo, X., 2022. Recent advancements on three-dimensional electrospun nanofiber scaffolds for tissue engineering. Adv. Fiber Mater. 4, 959–986. https://doi.org/10.1007/s42765-022-00170-7.

Chen, X., Gao, C., Jiang, J., Wu, Y., Zhu, P., Chen, G., 2019. 3D printed porous PLA/nHA composite Scaffolds with enhanced osteogenesis and osteoconductivity in vivo for bone regeneration. Biomed. Mater. 14, 065003. https://doi.org/10.1088/1748-605X/ab388d.

Davachi, S.M., Kaffashi, B., Torabinejad, B., Zamanian, A., 2016. In-vitro investigation and hydrolytic degradation of antibacterial nanocomposites based on PLLA/Triclosan/Nano-Hydroxyapatite. Polymer 83, 101–110. https://doi.org/10.1016/j.polymer.2015.12.015.

Di Lorenzo, M.L., Androsch, R., 2019. Influence of A′-/A-crystal Polymorphism on Properties of Poly(L -lactic Acid). Polym. Int. 68, 320–334. https://doi.org/10.1002/pi.5707.

Díaz, E., Molpeceres, A.L., Sandonis, I., Puerto, I., 2019. PLLA/nHA composite films and scaffolds for medical implants: in vitro degradation, thermal and mechanical properties. J. Inorg. Organomet Polym. 29, 121–131. https://doi.org/10.1007/

s10904-018-0972-y.
Eling, B., Gogolewski, S., Pennings, A.J., 1982. Biodegradable materials of poly(l-Lactic Acid): 1. Melt-spun and solution-spun fibres. Polymer 23, 1587–1593. https://doi.org/10.1016/0032-3861(82)90176-8.
Farag, M.M., 2023. Recent trends on biomaterials for tissue regeneration applications: review. J. Mater. Sci. 58, 527–558. https://doi.org/10.1007/s10853-022-08102-x.
Fendi, F., Abdullah, B., Suryani, S., Usman, A.N., Tahir, D., 2024. Development and application of hydroxyapatite-based scaffolds for bone tissue regeneration: a systematic literature review. Bone 183, 117075. https://doi.org/10.1016/j.bone.2024.117075.
Fernandez-Yague, M.A., Abbah, S.A., McNamara, L., Zeugolis, D.I., Pandit, A., Biggs, M.J., 2015. Biomimetic approaches in bone tissue engineering: integrating biological and physicomechanical strategies. Adv. Drug Deliv. Rev. 84, 1–29. https://doi.org/10.1016/j.addr.2014.09.005.
Glimcher, M.J., 1959. Molecular biology of mineralized tissues with particular reference to bone. Rev. Mod. Phys. 31, 359–393. https://doi.org/10.1103/RevModPhys.31.359.
Hambleton, A.R., Mele, E., 2024. Dimensional and structural instability of electrospun polylactic acid membranes in liquid environments: role of water, ethanol, and temperature. Fibers Polym. https://doi.org/10.1007/s12221-024-00564-x.
Hong, Z., Reis, R.L., Mano, J.F., 2008. Preparation and in vitro characterization of scaffolds of poly(l-lactic acid) containing bioactive glass ceramic nanoparticles. Acta Biomater. 4, 1297–1306. https://doi.org/10.1016/j.actbio.2008.03.007.
Hoogsteen, W., Postema, A.R., Pennings, A.J., Ten Brinke, G., Zugenmaier, P., 1990. Crystal structure, conformation and morphology of solution-spun poly(L-Lactide) fibers. Macromolecules 23, 634–642. https://doi.org/10.1021/ma00204a041.
Hotaling, N.A., Bharti, K., Kriel, H., Simon, C.G., 2015. DiameterJ: a validated open source nanofiber diameter measurement tool. Biomaterials 61, 327–338. https://doi.org/10.1016/j.biomaterials.2015.05.015.
Huang, X., Lou, Y., Duan, Y., Liu, H., Tian, J., Shen, Y., Wei, X., 2024. Biomaterial scaffolds in maxillofacial bone tissue engineering: a review of recent advances. Bioact. Mater. 33, 129–156. https://doi.org/10.1016/j.bioactmat.2023.10.031.
Hwangbo, H., Lee, J., Kim, G., 2022. Mechanically and biologically enhanced 3D-printed HA/PLLA/dECM biocomposites for bone tissue engineering. Int. J. Biol. Macromol. 218, 9–21. https://doi.org/10.1016/j.ijbiomac.2022.07.040.
Ielo, I., Calabrese, G., De Luca, G., Conoci, S., 2022. Recent advances in hydroxyapatite-based biocomposites for bone tissue regeneration in orthopedics. IJMS 23, 9721. https://doi.org/10.3390/ijms23179721.
Jeznach, O., Kołbuk, D., Reich, T., Sajkiewicz, P., 2022. Immobilization of gelatin on fibers for tissue engineering applications: a comparative study of three aliphatic polyesters. Polymers 14, 4154. https://doi.org/10.3390/polym14194154.
Kapat, K., Shubhra, Q.T.H., Zhou, M., Leeuwenburgh, S., 2020. Piezoelectric nano-biomaterials for biomedicine and tissue regeneration. Adv. Funct. Mater. 30, 1909045. https://doi.org/10.1002/adfm.201909045.
Karbowniczek, J.E., Ura, D.P., Stachewicz, U., 2022. Nanoparticles distribution and agglomeration analysis in electrospun fiber based composites for desired mechanical performance of poly(3-Hydroxybuty-rate-Co-3-hydroxyvalerate (PHBV) scaffolds with hydroxyapatite (HA) and titanium dioxide (TiO2) towards medical applications. Compos. Part B: Eng. 241, 110011. https://doi.org/10.1016/j.compositesb.2022.110011.
Kennedy, S.M., Vasanthanathan, A., Robert Rb, J., Amudhan, K., 2024. Advancements and prospects of polymer-based hybrid composites for bone plate applications. Polym. -Plast. Technol. Mater. 63, 68–87. https://doi.org/10.1080/25740881.2023.2274564.
Khouri, N.G., Bahú, J.O., Blanco-Llamero, C., Severino, P., Concha, V.O.C., Souto, E.B., 2024. Polylactic acid (PLA): properties, synthesis, and biomedical applications – a review of the literature. J. Mol. Struct. 1309, 138243. https://doi.org/10.1016/j.molstruc.2024.138243.
Kleintjens, L.A., 2012. Integration of Fundamental Polymer Science and Technology. Springer Science & Business Media. ISBN 978-94-009-4185-4.
Kołbuk, D., Ciechomska, M., Jeznach, O., Sajkiewicz, P., 2022. Effect of crystallinity and related surface properties on gene expression of primary fibroblasts. RSC Adv. 12, 4016–4028. https://doi.org/10.1039/D1RA07237D.
Koons, G.L., Diba, M., Mikos, A.G., 2020. Materials design for bone-tissue engineering. Nat. Rev. Mater. 5, 584–603. https://doi.org/10.1038/s41578-020-0204-2.
Leroy, A., Ribeiro, S., Grossiord, C., Alves, A., Vestberg, R.H., Salles, V., Brunon, C., Gritsch, K., Grosgogeat, B., Bayon, Y., 2017. FTIR microscopy contribution for comprehension of degradation mechanisms in PLA-based implantable medical devices. J. Mater. Sci: Mater. Med 28, 87. https://doi.org/10.1007/s10856-017-5894-7.
Li, Liao, 2019. Tjong electrospun polyvinylidene fluoride-based fibrous scaffolds with piezoelectric characteristics for bone and neural tissue engineering. Nanomaterials 9, 952. https://doi.org/10.3390/nano9070952.
Li, X., Liu, H., Wang, J., Li, C., 2012. Preparation and characterization of PLLA/nHA nonwoven Mats via laser melt electrospinning. Mater. Lett. 73, 103–106. https://doi.org/10.1016/j.matlet.2011.12.108.
Li, J., Zhao, Y., Zhai, W., Zhao, X., Dai, K., Liu, C., Shen, C., 2024. Highly aligned electrospun film with wave-like structure for multidirectional strain and visual sensing. Chem. Eng. J. 485, 149952. https://doi.org/10.1016/j.cej.2024.149952.
Liao, S., Tamura, K., Zhu, Y., Wang, W., Uo, M., Akasaka, T., Cui, F., Watari, F., 2006. Human neutrophils reaction to the biodegraded nano-hydroxyapatite/collagen and nano-hydroxyapatite/collagen/poly(L -lactic Acid) composites. J. Biomed. Mater. Res. 76A, 820–825. https://doi.org/10.1002/jbm.a.30582.
Liu, Y., Guo, Q., Zhang, X., Wang, Y., Mo, X., Wu, T., 2023. Progress in electrospun fibers for manipulating cell behaviors. Adv. Fiber Mater. 5, 1241–1272. https://doi.org/10.1007/s42765-023-00281-9.
Liu, X., Hua, X., Wu, H., 2024. Degradation behavior of poly (lactic acid) during accelerated photo-oxidation: insights into structural evolution and mechanical properties. J. Polym. Environ. https://doi.org/10.1007/s10924-024-03211-x.
Liu, J., Zhang, S., Zhang, L., Liu, L., Bai, Y., 2014. Uniaxial stretching of polylactide with different initial crystalline morphologies and temperature effect. Eur. Polym. J. 61, 83–92. https://doi.org/10.1016/j.eurpolymj.2014.08.021.
Lopresti, F., Carfì Pavia, F., Vitrano, I., Kersaudy-Kerhoas, M., Brucato, V., La Carrubba, V., 2020. Effect of hydroxyapatite concentration and size on morpho-mechanical properties of PLA-based randomly oriented and aligned electrospun nanofibrous mats. J. Mech. Behav. Biomed. Mater. 101, 103449. https://doi.org/10.1016/j.jmbbm.2019.103449.
Manzini, B.M., Machado, L.M.R., Noritomi, P.Y., Da Silva, J.V.L., 2021. Advances in bone tissue engineering: a fundamental review. J. Biosci. 46, 17. https://doi.org/10.1007/s12038-020-00122-6.
Moradi, A., Szewczyk, P.K., Stachewicz, U., 2023. Bridging a gap in thermal conductivity and heat transfer in hybrid fibers and yarns via polyimide and silicon nitride composites. Small 19, 2305104. https://doi.org/10.1002/smll.202305104.
Nagai, A., Yamashita, K., Imamura, M., Azuma, H., 2008. Hydroxyapatite electret accelerates reendothelialization and attenuates intimal hyperplasia occurring after endothelial removal of the rabbit carotid artery. Life Sci. 82, 1162–1168. https://doi.org/10.1016/j.lfs.2008.03.017.
Nasker, P., Samanta, A., Rudra, S., Sinha, A., Mukhopadhyay, A.K., Das, M., 2019. Effect of fluorine substitution on sintering behaviour, mechanical and bioactivity of hydroxyapatite. J. Mech. Behav. Biomed. Mater. 95, 136–142. https://doi.org/10.1016/j.jmbbm.2019.03.032.
Nazir, F., Iqbal, M., Khan, A.N., Mazhar, M., Hussain, Z., 2021. Fabrication of Robust Poly L-lactic acid/cyclic olefinic copolymer (PLLA/COC) blends: study of physical properties, structure, and cytocompatibility for bone tissue engineering. J. Mater. Res. Technol. 13, 1732–1751. https://doi.org/10.1016/j.jmrt.2021.05.073.
Norouzi, S., Saveh Shemshaki, N., Norouzi, E., Latifi, M., Azimi, B., Danti, S., Qiao, X., Miao, Y., Yang, S., Gorji, M., et al., 2024. Recent advances in biomaterials for tissue-engineered constructs: essential factors and engineering techniques. Mater. Today Chem. 37, 102016. https://doi.org/10.1016/j.mtchem.2024.102016.
Obregon, N., Agubra, V., Pokhrel, M., Campos, H., Flores, D., De La Garza, D., Mao, Y., Macossay, J., Alcoutlabi, M., 2016. Effect of polymer concentration, rotational speed, and solvent mixture on fiber formation using forcespinning®. Fibers 4, 20. https://doi.org/10.3390/fib4020020.
Okabayashi, R., Nakamura, M., Okabayashi, T., Tanaka, Y., Nagai, A., Yamashita, K., 2009. Efficacy of polarized hydroxyapatite and silk fibroin composite dressing gel on epidermal recovery from full-thickness skin wounds. J. Biomed. Mater. Res 90B, 641–646. https://doi.org/10.1002/jbm.b.31329.
Pan, P., Kai, W., Zhu, B., Dong, T., Inoue, Y., 2007. Polymorphous crystallization and multiple melting behavior of poly(L -Lactide): molecular weight dependence. Macromolecules 40, 6898–6905. https://doi.org/10.1021/ma071258d.
Pan, P., Yang, J., Shan, G., Bao, Y., Weng, Z., Cao, A., Yazawa, K., Inoue, Y., 2012. Temperature-variable FTIR and solid-state ^{13}C NMR investigations on crystalline structure and molecular dynamics of polymorphic poly(L -Lactide) and poly(L -Lactide)/poly(D -Lactide) stereocomplex. Macromolecules 45, 189–197. https://doi.org/10.1021/ma201906a.
Panda, A.K., Sitaramgupta, V.S.N., Pandya, H.J., Basu, B., 2022. Electrical stimulation waveform-dependent osteogenesis on PVDF/BaTiO $_3$ composite using a customized and programmable cell stimulator. Biotech. Bioeng. 119, 1578–1597. https://doi.org/10.1002/bit.28076.
Paragkumar N, T., Edith, D., Six, J.-L., 2006. Surface characteristics of PLA and PLGA films. Appl. Surf. Sci. 253, 2758–2764. https://doi.org/10.1016/j.apsusc.2006.05.047.
Pariy, I.O., Chernozem, R.V., Chernozem, P.V., Mukhortova, Y.R., Skirtach, A.G., Shvartsman, V.V., Lupascu, D.C., Surmeneva, M.A., Mathur, S., Surmenev, R.A., 2022. Hybrid biodegradable electrospun scaffolds based on poly(l-Lactic Acid) and reduced graphene oxide with improved piezoelectric response. Polym. J. 54, 1237–1252. https://doi.org/10.1038/s41428-022-00669-1.
Patel, P.R., Gundloori, R.V.N., 2023. A review on electrospun nanofibers for multiple biomedical applications. Polym. Adv. Techs 34, 44–63. https://doi.org/10.1002/pat.5896.
Pathak, R., Punetha, V.D., Bhatt, S., Punetha, M., 2023. Multifunctional role of carbon dot-based polymer nanocomposites in biomedical applications: a review. J. Mater. Sci. 58, 6419–6443. https://doi.org/10.1007/s10853-023-08408-4.
Polak, M., Berniak, K., Szewczyk, P.K., Karbowniczek, J.E., Marzec, M.M., Stachewicz, U., 2023. PLLA Scaffolds with controlled surface potential and piezoelectricity for enhancing cell adhesion in tissue engineering. Appl. Surf. Sci. 621, 156835. https://doi.org/10.1016/j.apsusc.2023.156835.
Puiggali, J., Ikada, Y., Tsuji, H., Cartier, L., Okihara, T., Lotz, B., 2000. The frustrated structure of poly(l -Lactide). Polymer 41, 8921–8930. https://doi.org/10.1016/S0032-3861(00)00235-4.
Pyda, M., Czerniecka-Kubicka, A., 2017. Thermal Properties and Thermodynamics of Poly (l-Lactic Acid) (Advances in Polymer Science). In: Di Lorenzo, M.L., Androsch, R. (Eds.)Synthesis, Structure and Properties of Poly(lactic acid), 279. Springer International Publishing, Cham, pp. 153–193. (Advances in Polymer Science).
Qin, L., Yang, S., Zhao, C., Yang, J., Li, F., Xu, Z., Yang, Y., Zhou, H., Li, K., Xiong, C., et al., 2024. Prospects and challenges for the application of tissue engineering technologies in the treatment of bone infections. Bone Res. 12, 28. https://doi.org/10.1038/s41413-024-00332-w.
Rachmawati, H., 2016. Curcumin-loaded PLA nanoparticles: formulation and physical evaluation. Sci. Pharm. 84, 191–202. https://doi.org/10.3797/scipharm.ISP.2015.10.
Rai, B., Teoh, S.H., Ho, K.H., 2005. An in vitro evaluation of PCL–TCP composites as delivery systems for platelet-rich plasma. J. Control. Release 107, 330–342. https://

doi.org/10.1016/j.jconrel.2005.07.002.
Rancan, F., Papakostas, D., Hadam, S., Hackbarth, S., Delair, T., Primard, C., Verrier, B., Sterry, W., Blume-Peytavi, U., Vogt, A., 2009. Investigation of polylactic acid (PLA) nanoparticles as drug delivery systems for local dermatotherapy. Pharm. Res 26, 2027–2036. https://doi.org/10.1007/s11095-009-9919-x.
Ren, K., Shen, Y., Wang, Z.L., 2024. Piezoelectric properties of electrospun polymer nanofibers and related energy harvesting applications. Macro Mater. amp; Eng. 309, 2300307. https://doi.org/10.1002/mame.202300307.
Ribeiro, C., Sencadas, V., Costa, C.M., Gómez Ribelles, J.L., Lanceros-Méndez, S., 2011. Tailoring the morphology and crystallinity of poly(L-Lactide Acid) electrospun membranes. Sci. Technol. Adv. Mater. 12, 015001. https://doi.org/10.1088/1468-6996/12/1/015001.
Righetti, M.C., Gazzano, M., Di Lorenzo, M.L., Androsch, R., 2015. Enthalpy of melting of A′- and α-crystals of poly(l-Lactic Acid). Eur. Polym. J. 70, 215–220. https://doi.org/10.1016/j.eurpolymj.2015.07.024.
Rudawska, A., Jacniacka, E., 2009. Analysis for determining surface free energy uncertainty by the owen–wendt method. Int. J. Adhes. Adhes. 29, 451–457. https://doi.org/10.1016/j.ijadhadh.2008.09.008.
Salerno, A., Netti, P.A., 2023. Review on bioinspired design of ECM-mimicking scaffolds by computer-aided assembly of cell-free and cell laden micro-modules. JFB 14, 101. https://doi.org/10.3390/jfb14020101.
Saurav, S., Mohan, A., Tabassum, Z., Girdhar, M., 2024. Recent trends in polymer-based nanocomposites and its application in bone tissue engineering. Hyderabad, India 030138.
Saxena, A., Pandey, M., Dubey, A.K., 2019. Induced electroactive response of hydroxyapatite: a review. J. Indian Inst. Sci. 99, 339–359. https://doi.org/10.1007/s41745-019-00117-9.
Scaffaro, R., Lopresti, F., Botta, L., 2017. Preparation, characterization and hydrolytic degradation of PLA/PCL Co-Mingled nanofibrous mats prepared via dual-jet electrospinning. Eur. Polym. J. 96, 266–277. https://doi.org/10.1016/j.eurpolymj.2017.09.016.
Scaffaro, R., Settanni, L., Gulino, E.F., 2023. Release profiles of carvacrol or chlorhexidine of PLA/graphene nanoplatelets membranes prepared using electrospinning and solution blow spinning: a comparative study. Molecules 28, 1967. https://doi.org/10.3390/molecules28041967.
Sethu, S., Kalimuthu, M., Nagarajan, R., Krishnan, K., Mohammad, F., Arul Kumar, M., 2024. Hybrid fabrication and characterization of biocompatible bamboo/PLA composites. J. Mater. Res. Technol. 29, 2656–2666. https://doi.org/10.1016/j.jmrt.2024.01.265.
Shehata, N., Elnabawy, E., Abdelkader, M., Hassanin, A., Salah, M., Nair, R., Ahmad Bhat, S., 2018. Static-aligned piezoelectric poly (vinylidene fluoride) electrospun nanofibers/MWCNT composite membrane: facile method. Polymers 10, 965. https://doi.org/10.3390/polym10090965.
Softas, C., 2022. Selective Laser Sintering of Hydroxyapatite-Based Materials for Tissue Engineering. In: Narayan, R.J. (Ed.), In *Additive Manufacturing in Biomedical Applications*. ASM International, pp. 92–105. ISBN 978-1-62708-392-8.
Srivastava, A., Bhati, P., Singh, S., Agrawal, M., Kumari, N., Vashisth, P., Chauhan, P., Bhatnagar, N., 2024. A review on polylactic acid-based blends/composites and the role of compatibilizers in biomedical engineering applications. Polym. Eng. Sci. 64, 1003–1044. https://doi.org/10.1002/pen.26626.
Stoch, A., Jastrzębski, W., Brożek, A., Stoch, J., Szaraniec, J., Trybalska, B., Kmita, G., 2000. FTIR absorption–reflection study of biomimetic growth of phosphates on titanium implants. J. Mol. Struct. 555, 375–382. https://doi.org/10.1016/S0022-2860(00)00623-2.
Sukumaran, S., Szewczyk, P.K., Knapczyk-Korczak, J., Stachewicz, U., 2023. Optimizing piezoelectric coefficient in PVDF fibers: key strategies for energy harvesting and smart textiles. Adv. Electron. Mater. 9, 2300404. https://doi.org/10.1002/aelm.202300404.
Szewczyk, P.K., Taşlı, A.E., Knapczyk-Korczak, J., Stachewicz, U., 2023. Steering triboelectric and mechanical properties of polymer fibers with carbon black. Compos. Sci. Technol. 243, 110247. https://doi.org/10.1016/j.compscitech.2023.110247.
Szewczyk, P.K., Ura, D.P., Metwally, S., Knapczyk-Korczak, J., Gajek, M., Marzec, M.M., Bernasik, A., Stachewicz, U., 2019. Roughness and fiber fraction dominated wetting of electrospun fiber-based porous meshes. Polymers 11, 34. https://doi.org/10.3390/polym11010034.
Tamayol, A., Akbari, M., Annabi, N., Paul, A., Khademhosseini, A., Juncker, D., 2013. Fiber-based tissue engineering: progress, challenges, and opportunities. Biotechnol. Adv. 31, 669–687. https://doi.org/10.1016/j.biotechadv.2012.11.007.
Tazibt, N., Kaci, M., Dehouche, N., Ragoubi, M., Atanase, L.I., 2023. Effect of filler content on the morphology and physical properties of poly(lactic acid)-hydroxyapatite composites. Materials 16, 809. https://doi.org/10.3390/ma16020809.
Van Manen, E.H.C., Zhang, W., Walboomers, X.F., Vazquez, B., Yang, F., Ji, W., Yu, N., Spear, D.J., Jansen, J.A., Yelick, P.C., 2014. The influence of electrospun fibre scaffold orientation and nano-hydroxyapatite content on the development of tooth bud stem cells in vitro. Odontology 102, 14–21. https://doi.org/10.1007/s10266-012-0087-9.
Vijayendran, B.R., 1979. Polymer polarity and surfactant adsorption. J. Appl. Polym. Sci. 23, 733–742. https://doi.org/10.1002/app.1979.070230308.
Wang, X., Kumar, V., Li, W., 2007. Low density sub-critical CO_2 -blown solid-state PLA foams. Cell. Polym. 26, 11–35. https://doi.org/10.1177/026248930702600102.
Wang, P., Lv, H., Cao, X., Liu, Y., Yu, D.-G., 2023. Recent progress of the preparation and application of electrospun porous nanofibers. Polymers 15, 921. https://doi.org/10.3390/polym15040921.
Wasanasuk, K., Tashiro, K., 2011. Crystal structure and disorder in poly(l-Lactic Acid) δ Form (A′ Form) and the phase transition mechanism to the ordered α form. Polymer 52, 6097–6109. https://doi.org/10.1016/j.polymer.2011.10.046.
Winey, K.I., Vaia, R.A., 2007. Polymer nanocomposites. MRS Bull. 32, 314–322. https://doi.org/10.1557/mrs2007.229.
Wortham, J.M., Haddad, M.B., Stewart, R.J., Annambhotla, P., Basavaraju, S.V., Nabity, S.A., Griffin, I.S., McDonald, E., Beshearse, E.M., Grossman, M.K., et al., 2024. Second nationwide tuberculosis outbreak caused by bone allografts containing live cells — United States, 2023. MMWR Morb. Mortal. Wkly. Rep. 72, 1385–1389. https://doi.org/10.15585/mmwr.mm725253a1.
Wunderlich, B., Grebowicz, J., 1984. Thermotropic Mesophases and Mesophase Transitions of Linear, Flexible Macromolecules (Advances in Polymer Science). In: Platé, N.A. (Ed.)Liquid Crystal Polymers II/III, 60/61. Springer Berlin Heidelberg, Berlin, Heidelberg, pp. 1–59. (Advances in Polymer Science).
Xing, J., Zhang, M., Liu, X., Wang, C., Xu, N., Xing, D., 2023. Multi-material electrospinning: from methods to biomedical applications. Mater. Today Bio 21, 100710. https://doi.org/10.1016/j.mtbio.2023.100710.
Yanagida, H., Okada, M., Masuda, M., Ueki, M., Narama, I., Kitao, S., Koyama, Y., Furuzono, T., Takakuda, K., 2009. Cell adhesion and tissue response to hydroxyapatite nanocrystal-coated poly(l-lactic acid) fabric. J. Biosci. Bioeng. 108, 235–243. https://doi.org/10.1016/j.jbiosc.2009.04.003.
Yang, X., Chen, Y., Zhang, C., Duan, G., Jiang, S., 2023. Electrospun carbon nanofibers and their reinforced composites: preparation, modification, applications, and perspectives. Compos. Part B: Eng. 249, 110386. https://doi.org/10.1016/j.compositesb.2022.110386.
Zaszczyńska, A., Gradys, A., Ziemiecka, A., Szewczyk, P.K., Tymkiewicz, R., Lewandowska-Szumieł, M., Stachewicz, U., Sajkiewicz, P., 2024a. Enhanced electroactive phases of poly(vinylidene fluoride) fibers for tissue engineering applications. IJMS 25, 4980. https://doi.org/10.3390/ijms25094980.
Zaszczyńska, A., Kołbuk, D., Gradys, A., Sajkiewicz, P., 2024b. Development of poly (Methyl methacrylate)/nano-hydroxyapatite (PMMA/nHA) nanofibers for tissue engineering regeneration using an electrospinning technique. Polymers 16, 531. https://doi.org/10.3390/polym16040531.
Zaszczyńska, A., Niemczyk-Soczynska, B., Sajkiewicz, P., 2022. A comprehensive review of electrospun fibers, 3D-printed scaffolds, and hydrogels for cancer therapies. Polymers 14, 5278. https://doi.org/10.3390/polym14235278.
Zhang, J., Duan, Y., Domb, A.J., Ozaki, Y., 2010. PLLA mesophase and its phase transition behavior in the PLLA−PEG−PLLA copolymer as revealed by infrared spectroscopy. Macromolecules 43, 4240–4246. https://doi.org/10.1021/ma100301h.
Zhang, J., Duan, Y., Sato, H., Tsuji, H., Noda, I., Yan, S., Ozaki, Y., 2005. Crystal modifications and thermal behavior of poly(L -Lactic Acid) revealed by infrared spectroscopy. Macromolecules 38, 8012–8021. https://doi.org/10.1021/ma051232r.
Zhang, R., Ma, P.X., 1999. Porous poly(L-Lactic Acid)/apatite composites created by biomimetic process. J. Biomed. Mater. Res. 45, 285–293. https://doi.org/10.1002/(SICI)1097-4636(19990615)45:4<285::AID-JBM2>3.0.CO;2-2.
Zhang, J., Tashiro, K., Domb, A.J., Tsuji, H., 2006. Confirmation of disorder α form of poly (L -lactic Acid) by the x-ray fiber pattern and polarized IR/Raman spectra measured for uniaxially-oriented samples. Macromol. Symp. 242, 274–278. https://doi.org/10.1002/masy.200651038.
Zhang, Y., Wang, W., Chen, Z., Shi, H., Zhang, W., Zhang, X., Hua, X., 2023b. An artificial bone filling material of poly L-lactic acid/collagen/nano-hydroxyapatite microspheres: preparation and collagen regulation on the property. Int. J. Biol. Macromol. 229, 35–50. https://doi.org/10.1016/j.ijbiomac.2022.12.200.
Zhang, M., Xu, F., Cao, J., Dou, Q., Wang, J., Wang, J., Yang, L., Chen, W., 2024. Research advances of nanomaterials for the acceleration of fracture healing. Bioact. Mater. 31, 368–394. https://doi.org/10.1016/j.bioactmat.2023.08.016.
Zhang, M., Xu, S., Wang, R., Che, Y., Han, C., Feng, W., Wang, C., Zhao, W., 2023a. Electrospun nanofiber/hydrogel composite materials and their tissue engineering applications. J. Mater. Sci. Technol. 162, 157–178. https://doi.org/10.1016/j.jmst.2023.04.015.
Zhao, G., Huang, B., Zhang, J., Wang, A., Ren, K., Wang, Z.L., 2017. Electrospun poly(l -Lactic Acid) nanofibers for nanogenerator and diagnostic sensor applications. Macro Mater. amp; Eng. 302, 1600476. https://doi.org/10.1002/mame.201600476.
Zhao, H., Liang, K., Wang, S., Ding, Z., Huang, X., Chen, W., Ren, Y., Li, J., 2023. A stress self-adaptive silicon/carbon “ordered structures” to suppress the electro-chemo-mechanical failure: piezo-electrochemistry and piezo-ionic dynamics. Adv. Sci. 10, 2303696. https://doi.org/10.1002/advs.202303696.
Zhou, W., Yu, J., Zhang, S., 2023. Environmentally friendly waterproof and breathable membranes via electrospinning. J. Text. Inst. 1–23. https://doi.org/10.1080/00405000.2023.2201061.
Zhu, Y., Goh, C., Shrestha, A., 2021b. Biomaterial properties modulating bone regeneration. Macromol. Biosci. 21, 2000365. https://doi.org/10.1002/mabi.202000365.
Zhu, G., Zhang, T., Chen, M., Yao, K., Huang, X., Zhang, B., Li, Y., Liu, J., Wang, Y., Zhao, Z., 2021a. Bone physiological microenvironment and healing mechanism: basis for future bone-tissue engineering Scaffolds. Bioact. Mater. 6, 4110–4140. https://doi.org/10.1016/j.bioactmat.2021.03.043.